



CCM2 deficient endothelial cells undergo a ROCK dependent reprogramming into senescence associated secretory phenotype

Daphné Raphaëlle Vannier, Apeksha Shapeti, Florent Chuffart, Emmanuelle Planus, Sandra Manet, Paul Rivier, Olivier Destaing, Corinne Albiges-Rizo, Hans van Oosterwyck, Eva Faurobert

► To cite this version:

Daphné Raphaëlle Vannier, Apeksha Shapeti, Florent Chuffart, Emmanuelle Planus, Sandra Manet, et al.. CCM2 deficient endothelial cells undergo a ROCK dependent reprogramming into senescence associated secretory phenotype. *Angiogenesis*, 2021, <10.1007/s10456-021-09809-2>. <hal-03437734>

HAL Id: hal-03437734

<https://hal.science/hal-03437734v1>

Submitted on 20 Nov 2021

HAL is a multi-disciplinary open access archive for the deposit and dissemination of scientific research documents, whether they are published or not. The documents may come from teaching and research institutions in France or abroad, or from public or private research centers.

L'archive ouverte pluridisciplinaire **HAL**, est destinée au dépôt et à la diffusion de documents scientifiques de niveau recherche, publiés ou non, émanant des établissements d'enseignement et de recherche français ou étrangers, des laboratoires publics ou privés.



HAL Authorization

CCM2 deficient endothelial cells undergo a ROCKs dependent reprogramming into senescence associated secretory phenotype.

Daphné Raphaëlle Vannier¹, Apeksha Shapeti^{2,3}, Florent Chuffart¹, Emmanuelle Planus¹, Sandra Manet^{1†}, Paul Rivier¹, Olivier Destaing¹, Corinne Albiges-Rizo^{1*}, Hans Van Oosterwyck^{2,3*} and Eva Faurobert^{1*✉}.

1 Institute for Advanced Biosciences, University Grenoble Alpes, INSERM U1209, CNRS UMR5309, site santé, Allée des Alpes 38042 Grenoble, France

2 Biomechanics Section (BMe), Department of Mechanical Engineering, KU Leuven, Leuven, Belgium.

3 Prometheus, div. Skeletal Tissue Engineering, KU Leuven, Leuven, Belgium.

† Deceased

*Co-last authors

✉ corresponding author. E-mail for correspondance: eva.fauRobert@univ-grenoble-alpes.fr

Abstract:

Cerebral Cavernous Malformation (CCM) is a cerebrovascular disease in which stacks of dilated haemorrhagic capillaries form focally in the brain. Whether and how defective mechanotransduction, cellular mosaicism and inflammation interplay to sustain the progression of CCM disease is unknown. Here, we reveal that CCM1- and CCM2-silenced endothelial cells expanded *in vitro* enter into senescence-associated secretory phenotype (SASP) that they use to invade the extracellular matrix and attract surrounding wild-type endothelial and immune cells. Further, we demonstrate that this SASP is driven by the cytoskeletal, molecular and transcriptomic disorders provoked by ROCKs dysfunctions. By this, we propose that CCM2 and ROCKs could be parts of a scaffold controlling senescence, bringing new insights into the emerging field of the control of aging by cellular mechanics. These *in vitro* findings reconcile the known dysregulated traits of CCM2-deficient endothelial cells into a unique endothelial fate. Based on these *in vitro* results, we propose that a SASP could link the increased ROCK-dependent cell contractility in CCM2-deficient ECs with microenvironment remodelling and long-range chemo-attraction of endothelial and immune cells.

19 Introduction:

20 Cerebral Cavernous malformations (CCM) are stacks of overgrown, dilated and haemorrhagic
21 venous capillaries formed by a unique layer of poorly joined endothelial cells (ECs) without
22 intervening cerebral mural cells(1). Loss-of-function mutations on 3 genes (*CCM1/KRIT*,
23 *CCM2/Malcavernin*, *CCM3/PDCD10*) are associated with the familial form of the disease(2,3).
24 *CCM1* or *CCM2*-associated disease develops later in life than *CCM3* which is a more aggressive
25 form of the disease(4,5).

26 CCM lesions expand with time and they become infiltrated by immune cells that sustain a
27 chronic inflammatory response(6,7). Intriguingly, CCM lesions are composed of a mosaic of
28 mutant and wild-type ECs (8–11). Malinverno and colleagues have further shown that the
29 majority of ECs bordering large mature ccm3 caverns are actually wild-type ECs that have been
30 attracted to the lesion site at least in part by mutant ECs(11). Other studies have reported that
31 *CCM* mutant ECs secrete metalloproteases(12–14) or cytokines(15), over-produce ROS(16),
32 present defective autophagy(17) or that they undergo an endothelial to mesenchymal transition
33 (EndMT)(18). Moreover, loss of CCM proteins activates $\beta 1$ integrin (19,20), p38 MAPK(21),
34 ERK5-KLF2/4(20,22,23) and TLR4 signaling pathways(24). However, how these various
35 dysregulations interplay to generate CCM lesions is not well known.

36 A remarkable feature of CCM lesions is their peculiar mechanical microenvironment. Indeed,
37 ECs in CCM lesions experience disturbed forces coming from stagnant blood flow(25) on their
38 luminal side and increased ECM stiffness upon matrix remodelling on their basal side(19).
39 Increased RhoA/ROCK-dependent intracellular tension (19) is a conserved feature of *CCM*
40 mutant ECs in humans and animal models (13,26–28). ROCK overactivation stimulates the
41 polymerization of a contractile acto-myosin cytoskeleton that shifts the tensional homeostasis
42 between cell-cell and cell-extracellular matrix (ECM) adhesions. We previously showed that
43 the endothelial tensional homeostasis is actually under the control of the coupled activities of
44 the two ROCK isoforms(29). The molecular scaffold formed by the association of CCM1 and
45 CCM2 recruits ROCK2 to VE-cadherin complexes to promote the polymerization of a cortical
46 acto-myosin cytoskeleton supporting cell-cell junctions. At the same time, this CCM/ROCK2
47 complex keeps ROCK1 kinase activity low thereby limiting the adhesion of the cell to the ECM.
48 When the CCM1/2 complex is lost, ROCK2 delocalizes from VE-cadherin while ROCK1 gets
49 over activated and promotes the polymerization of numerous $\beta 1$ integrin-anchored acto-myosin
50 stress fibers that most likely tear the cell-cell junctions apart(29). Importantly, it is yet unknown
51 whether, beyond their role on the architecture of the endothelium, ROCKs are also involved in
52 the control of gene expression downstream of CCM2.

53 The mechanical defects play a primary role in the development of the disease. Inhibition of both
54 ROCKs with chemical inhibitors, among which fasudil, blocks the genesis and maturation of
55 CCM lesions in animal models(30–32). However, the toxicity of these drugs precludes their
56 use in patients. It is therefore critical to find new therapies targeting specific downstream
57 pathways. Toward this goal, we need to find a mechanistic explanation that could integrate all
58 the different dysregulated traits of *CCM* mutant ECs.

59 Here, we reveal that the transcriptome of CCM2-silenced ECs cultured *in vitro* presents a
60 signature of Senescence-Associated Secretory Phenotype (SASP). Cellular senescence
61 contributes to a wide variety of human age-related pathologies, including cancer, fibrosis,
62 cardiovascular diseases, or neurological disorders(33). We demonstrate that CCM2-silenced
63 ECs indeed enter into premature senescence and acquire degradative and invasive skills.
64 Moreover, CCM2-deficient ECs gain paracrine functions through secreted factors that are able
65 to attract *in vitro* wild-type ECs and immune cells. Remarkably, we show that this SASP is a
66 triggered by dysfunctional ROCK1 and ROCK2 and by increased ECs contractility. This
67 unexpected endothelial fate transition triggered by the loss of CCM2 reconciles all the known
68 dysregulated features of CCM2-deficient ECs. These features, if conserved *in vivo*, could
69 support the mosaicism of the CCM lesions and their inflammatory state.

Results:

1) The loss of CCM2 turns on a SASP transcriptomic program in endothelial cells.

KRIT and CCM2 proteins interact with each other to form a molecular scaffold(34). We previously showed that, owing to the stabilizing effect of CCM2 on KRIT, both proteins are lost when CCM2 is silenced(19). We therefore chose to silence CCM2 in order to deplete the entire KRIT/CCM2 complex. To study the gene expression program of a pure population of ECs depleted for CCM2, we performed RNA sequencing on monolayers of human umbilical vein endothelial cells (HUVECs) after two consecutive rounds of transfection with CCM2 targeting siRNA (siCCM2) or with non-targeting siRNA (siNT). CCM2 silencing was of 86% (figS1A) as reported in Lisowska et al., 2018(29). A total number of 2057 differentially expressed genes (DEGs) (fold change [FC] ≥ 2 ; $P < 0.05$, FDR corrected using Benjamini Hochberg method (35)) were identified in siCCM2-treated compared to siNT-treated HUVECs. Among these DEGs, 1316 upregulated while 739 were downregulated (Table S1).

To investigate the cellular functions altered by the loss of CCM2, we performed a Gene Ontology analysis on these DEGs using cellular component (Fig 1A) and biological process (Fig 1B) annotations (Table S2). Up-regulated genes were associated with the plasma membrane, secretory vesicles, extracellular matrix and focal adhesions (Fig 1A). They related to ECM organization, cell adhesion and migration, secretion, inflammatory response to cytokines and calcium homeostasis (Fig1B). Down-regulated genes were associated with the nuclear part of the cell, chromosomes, chromatin, the mitotic spindle pole, kinetochores and microtubules (Fig 1A). They relate to DNA replication, recombination and repair, chromosome segregation, microtubule-dependent movements and cell cycle progression (Fig 1B). A schematic representation of the enriched pathways found by a Reactome analysis in siCCM2 HUVEC is given in Figure 1C. In fact, these upregulated and downregulated functions (Fig 1B, C) evoke a striking unique cellular state; a senescence-associated secretory phenotype (SASP). This phenotype defines the ability of cell-cycle-arrested cells to secrete pro-inflammatory cytokines, chemokines, growth factors and proteases giving rise to ECM remodelling and to the stimulation of neighbour cells proliferation and invasiveness(36).

To test the hypothesis that a SASP transcriptomic program is turned on in siCCM2 HUVECs, we searched for specific transcriptomic signatures of senescence and SASP in the literature corresponding to gene sets enriched in senescent cells among which fibroblasts and endothelial cells(37–40). These gene sets relate to up- and down-regulated genes (Table S3). We then searched for an enrichment in these gene sets in the CCM2-depleted ECs transcriptome using Gene Set Enrichment Analysis (GSEA). We confirmed that these premature replicative senescence and SASP signatures are significantly enriched in the CCM2-silenced transcriptome (Fig1D, Fig S2). Overall, these functional analyses of the transcriptome suggest that ECs undergo a SASP when CCM2 is lost.

2) CCM2- and KRIT-depleted ECs display hallmarks of SASP.

Since a SASP transcriptomic program is turned on upon the loss of CCM2, we next sought for features of premature senescence in these cells. We looked for different hallmarks, as the combination of multiple traits is required to ascertain senescence(41). HUVECs were analysed at passage 4 when siNT cells are still proliferative and healthy. In addition to flattening and elongating upon the production of transversal stress fibers (Fig S5B), CCM2-depleted ECs expressed almost a 3-fold increase in lysosomal senescence-associated β -galactosidase (SA- β -gal) activity, the historical marker of senescence (Fig 2A, 2B). In addition, their nuclei displayed senescence-associated heterochromatin foci (SAHF) as revealed by spots in DAPI and HIRA staining (Fig 2C, 2D) and their area was increased (Fig 2E). As senescence leads to cell cycle arrest, we looked at the expression level of the cell cycle inhibitors CDKNs. Among them, p21/CIP1 and p15/INK4b were 3-fold upregulated (Fig 2F). On the contrary, cyclin-dependent kinase 1 (CDK1), its regulator CKS1B and cyclin 2A (CCN2A) as well as the transcription factor E2F1, a driver of S phase entry, were all dramatically downregulated (Fig S3). Using BrdU incorporation followed by cytometry analysis, we detected a 2-fold reduction in the percentage of cells in S phase and an accumulation in G1 indicative of a defect in the G1/S transition of the cell cycle (Fig 2G). This translated into a significantly lowered rate of proliferation of the ECs population as shown by impedance measurements (Fig 2H), and a two-fold lowered percentage of cells positive for the proliferative marker Ki67 (Fig 2I, 2J). Overall, the combination of all these traits confirms that the loss of CCM2 indeed induced premature senescence in HUVECs.

Senescent cells secrete paracrine factors that can promote tumor development *in vivo* by engaging deleterious inflammatory responses and malignant phenotypes such as proliferation and invasiveness (42). We found that siCCM2 treated HUVECs overexpressed ECM remodelling mediators including matrix proteins, metalloproteases of the MMP and ADAM families, the plasminogen activator uPA and cross-linking enzymes (Fig 2K). Moreover, they overexpress cytokines and inflammatory chemokines among which IL-1A and B, IL8, CXCL1, 2, CCL20 and EREG that are hallmarks of SASP (43) (Fig 2K).

Having shown that the loss of CCM2 leads to SASP in HUVECs, we wondered whether this would also be conserved in cerebral microvascular ECs (HBMVECs), an *in vitro* cellular model more closely related to CCM. We also wondered whether this SASP would be a common feature of ECs depleted for KRIT and CCM3. Therefore, each of these proteins was depleted in HUVECs and HBMVECs (Fig S1B) and the appearance of marks of senescence was analysed. Firstly, results in HBMVECs paralleled that in HUVECs (Fig 3) confirming that the loss of CCM2 also led to senescence in brain microvascular ECs. Moreover, KRIT-depleted HUVECs or HBMVECs displayed the same senescent phenotype as CCM2-depleted HUVECs or HBMVECs. We observed an increase in cells expressing SA- β -gal activity (Fig 3A-D) and HIRA nuclear foci (Fig 3E-H), and a decrease in Ki67-positive cells (Fig 3I-L). Moreover, their proliferation rate was consistently reduced (Fig 3M-N). Interestingly, CCM3-depleted HUVECs or HBMVECs did not display marks of senescence and behaved as control cells in these assays in good agreement with CCM3 distinct role in ECs biology and onset of the disease(44). They did not show increased SA- β gal activity (Fig 3A-D), nor HIRA nuclear foci (Fig 3E-H). They had a normal level of Ki67 positive cells (Fig 3I-L) and they did not

proliferate differently from control cells (Fig 3M-N). Therefore, consistently with their strong association and regulation of common signaling pathways (19,44), the loss of KRIT and CCM2 similarly lead to premature *in vitro* cellular senescence of brain microvascular ECs.

3) ROCK2 controls the SASP transcriptomic program of CCM2-depleted ECs

ROCK-dependent perturbations in the mechanotransduction of ECs have a major role in the genesis and progression of CCM lesions. Inhibition of ROCK is sufficient to block the formation and the maturation of CCM lesions (30–32). We previously showed that the CCM1/2 complex is a scaffold recruiting ROCK2 at VE-cadherin complexes thereby limiting ROCK1 kinase activity to maintain the tensional homeostasis between cell-cell and cell-ECM adhesions. This coordination between ROCK1 and ROCK2 activities preserve the integrity of the endothelial monolayer(29). However, it is yet unknown whether ROCKs are also involved in the control of gene expression downstream of CCM2 and in particular in the regulation of this SASP transcriptomic program. Hence, we analysed the contribution of ROCK1 and ROCK2 by performing RNA sequencing on monolayers of CCM2-silenced HUVECs that were additionally silenced for ROCK1 or ROCK2 or HUVECs silenced only for ROCK1 or ROCK2 (Fig S1A) in the same set of experiments as that shown in figure 1. We have previously shown that the additional depletion of ROCK1 but not ROCK2 restores the morphological defects of the CCM2-deficient HUVECs and their permeability barrier(29). Similar phenotypes were observed in HBMVECs (Fig S5A). Strikingly, 65% of the DEGs with $\log_2FC > 1$ had their expression significantly returned toward the control level by the additional silencing of ROCKs (Fig 4A, Table S4). The silencing of ROCK2 had a stronger restoring effect than that of ROCK1 on the number of restored genes (Fig 4A, Table S4) and their level of expression (Fig 4B). Importantly, silencing of ROCK2 alone had overall an opposite effect to that of CCM2 on gene expression (Fig 4B), suggesting that ROCK2 acquires a gain of transcriptional function when CCM2 is lost.

We then studied the restoring effect of ROCK1 or ROCK2 silencing on the biological functions perturbed by CCM2 depletion. Table S5 gives the Gene Ontology analysis of the biological functions of the DEGs restored by ROCK1 and ROCK2 (common DEGs) or restored specifically by ROCK1 or ROCK2. ROCK2 had a broad restoring effect on all the biological functions dysregulated upon the loss of CCM2. Figure 4C shows the heatmap of the expression of DEGs associated with GO biological processes found enriched in siCCM2 cells. The expression of DEGs related to the down-regulated nuclear functions in siCCM2 HUVECs was fully restored by ROCK2 depletion while ROCK1 depletion had only a partial effect. In addition, up-regulated peri-membrane functions were rescued by the silencing of ROCK2 to a higher extent than that of ROCK1 (Fig 4C). Going further, we focused on the effect of ROCKs on the signatures of senescence or SASP found in siCCM2 transcriptome. While these signatures of senescence were still present upon ROCK1 depletion, they were not anymore significantly enriched in HUVECs doubly silenced for CCM2 and ROCK2 (Fig 4D, Fig S2).

Overall, our transcriptomic data reveal that, beyond their role on the cytoskeletal homeostasis of the endothelial monolayer, ROCK2 and to a lesser extent ROCK1 has a massive effect on

the genes regulated by CCM2. These genes are involved in a transcriptomic program supporting the onset of SASP when CCM2 is lost.

4) ROCKs dysfunctions induce premature senescence in CCM2-depleted ECs.

Having shown that ROCKs mediate the expression of genes involved in SASP, we next asked whether dysfunctional ROCKs played a causal role in the entry into SASP of CCM2-depleted ECs. Additional silencing of ROCK1 or ROCK2 in HUVECs and HBMVECs was similarly efficient in preventing the appearance of most of the features of senescence tested i.e. SA- β -gal activity, HIRA-positive SAHF and restored normal level of Ki67+ cells (Fig 5A, B, C, F, Fig S6). However, ROCK2 silencing was more efficient in preventing the accumulation of HUVECs in the G1 phase of the cell cycle (Fig 5E). This effect of ROCK2 silencing is consistent with its higher efficiency in lowering the expression of p21/CIP1 and p15/INK4b (Fig 5D) and in restoring the gene expression of down-regulated cyclins and cyclin dependent kinases (Fig S3). Moreover, the silencing of ROCK2 and to a lesser extent that of ROCK1 lowered the expression of SASP factors, i.e. ECM remodelers or inflammatory chemokines (Fig 5G, H).

Our next goal was then to know whether the cytoskeletal defects provoked by dysregulated ROCK1 and ROCK2 play a direct role in the premature senescence of CCM2-depleted HUVECs. To answer this question, we treated siCCM2 HUVECs with blebbistatin, an inhibitor of myosin II that blocks cell contractility or with Y-27632, an inhibitor of ROCK1 and 2 kinase activities. Both treatments inhibited the production of transversal actin stress fibers found in siCCM2 HUVECs and siCCM2 HBMVECs and restored a more cortical actin rim alike the one observed in control HUVECs (Fig S5A, B). Interestingly, these treatments inhibited all the senescent traits studied above, i.e. high SA- β -gal activity, HIRA-positive SAHF and accumulation in G1 phase of the cell cycle and restored normal level of Ki67+ cells (Fig 5A, B, C, E, F; Fig S6). These results support the fact that increased contractility is involved in the premature senescence of CCM2-depleted ECs. Noticeably, blebbistatin and Y-27632 had no effect on siNT HUVECs in these assays (Fig S5C, D, and E).

Overall, these data reveal that dysregulated ROCK1 and ROCK2 functions together with increased cell contractility lead CCM2-depleted ECs to enter into a premature senescence.

5) ROCK1 mediates ECM degradation and supports invasiveness of CCM2-depleted ECs and neighbouring WT ECs.

Cancer cells undergoing SASP can promote tumour development through a juxtacrine effect on their microenvironment by secreting matrix metalloproteinases (MMPs) and ECM remodeling enzymes that facilitate tumour cell invasiveness and metastasis(42). Similar to cancer progression, the formation of CCM lesions could result from a SASP-dependent invasion of the brain tissue by ECs. Consistently, MMPs have been found around CCM lesions in human(14) and in mouse(13), or zebrafish models(22) and their upregulation plays a role in CCM defects (12,20). To know whether upregulated expression of SASP factors confers invasive skills to siCCM2 HUVECs, we tested the ability of these cells to degrade ECM and invade a 3D matrix. To visualize the degradation of the ECM, siRNA transfected HUVECs or HBMVECs were

cultured overnight on fluorescent gelatin. siNT ECs barely degraded the gelatin as expected for differentiated ECs (Fig 6A, B; Fig S7A, B). Conversely and consistently with their new SASP expression program, siCCM2 ECs degraded the gelatin through scratch zones appearing dark in the fluorescently labelled layer (Fig 6A; FigS7A). The linear shapes of these scratch zones suggested that they were produced under focal adhesions. They were dependent on the activity of MMPs as demonstrated by their complete disappearance upon MMP inhibitor GM-6001 treatment (Fig 6A, B). Together with blocking the mechanosensitive assembly of focal adhesions (Fig S5F), Y-27632 and blebbistatin blocked the degradation of gelatin (Fig 6A, B; Fig S7A, B). We previously showed that additional silencing of ROCK1, but not of ROCK2, limits excessive focal adhesion formation in siCCM2 ECs(29). Accordingly, only the additional depletion of ROCK1 inhibited ECM degradation by siCCM2 ECs (Fig 6A, B; Fig S7). Overall, these data show that ROCK1-dependent increase in cell contractility and in cell-ECM adhesive sites together with the overexpression of MMPs are responsible for the acquisition of ECM degradative skills by siCCM2 ECs.

We next tested whether these senescent ECs had acquired invasive skills. Consistently with Maddaluno et al. (18), these cells expressed mesenchymal markers suggestive of an invasive phenotype (Fig S8). Interestingly, the expression of the EndMT markers were returned toward siNT level by the additional silencing of ROCKs (Fig S8). To actually measure their 3D invasiveness, GFP-expressing siRNA treated HUVECs were plated on 3D-degradable polyethylene glycol gels (PEG). Invasive sprouts were imaged after 18 hours and the maximum invasion distance was quantified. siCCM2 HUVECs invaded the 3D gel twice as deep as siNT HUVECs (Fig 6D). Moreover, upon silencing of CCM2, the leading cells consistently detached from the multicellular sprouts and migrated independently (Fig 6C). Additional silencing of ROCK1 or blebbistatin treatment reduced the invasiveness of siCCM2 HUVECs to the level of siNT HUVECs and blocked the detachment of the leading EC whereas silencing of ROCK2 enhanced them (Fig 6C, D). This promotion of invasiveness upon ROCK2 additional depletion is consistent with their increased traction forces recorded in a previous work(29).

CCM lesions are mosaics of mutant and WT ECs as shown in human and murine lesions(9–11). Moreover, it has been shown that CCM3 KO ECs can attract WT ECs *in vivo* in the brain vasculature and *in vitro* on mixed monolayers(11). Therefore, we asked whether senescent siCCM2 HUVECs could also stimulate the sprouting of WT HUVECs when mixed together on the surface of 3D-PEG gels. Strikingly, we observed that RFP-expressing WT HUVECs invaded the gels twice as deep when they were mixed with GFP-expressing siCCM2 HUVECs as when mixed with GFP-expressing siNT HUVECs (Fig 6E, F). Interestingly, this increased invasion was significantly reduced when WT HUVECs were mixed with siCCM2+siROCK1 HUVECs but remained unchanged when they were mixed with siCCM2+siROCK2 HUVECs (Fig 6E, F).

Altogether, our results show that senescent siCCM2 HUVECs have acquired a ROCK1-dependent capacity to invade the ECM and to sustain the invasion by WT HUVECs.

6) ROCK2 mediates the expression of paracrine factors by CCM2-depleted ECs that chemo-attract WT ECs and immune cells.

Apart from remodelling their surrounding ECM, senescent cells secrete paracrine factors that have been shown to promote invasiveness of neighbouring cells and engage deleterious inflammatory responses (42). A chronic inflammation is observed at the site of human and murine CCM lesions through the recruitment of activated lymphocytes and monocytes(45). Our transcriptome analysis showed the upregulation of around 30 cytokines upon CCM2 loss that returned towards control level by ROCKs silencing (Fig 5H). These inflammatory cytokines have a broad spectrum of targets among immune cells and ECs and bear different roles on cell proliferation, differentiation and chemoattraction as summarized in table S6.

We first tested whether these secreted factors would have a long distance paracrine effect allowing the recruitment of WT ECs. We measured the capacity of a media conditioned by siCCM2 HUVECs to chemo-attract serum-starved WT HUVECs through a layer of Matrigel in a modified Boyden chamber measuring the impedance of cells. Remarkably, siCCM2-conditioned media significantly increased the speed of invasion of WT HUVECs through the Matrigel showing that chemo-attractive factors secreted by siCCM2 HUVECs could also attract ECs (Fig 6G). Interestingly, this effect was inhibited by ROCK2 but not ROCK1 additional silencing (Fig 6G). Therefore, siCCM2 HUVECs produce paracrine factors that attract WT ECs in a ROCK2-dependent manner.

We then tested whether the loss of CCM2 leads to the secretion of chemo-attractive cues for immune cells. Thus, we measured the capacity of media conditioned by siCCM2 HUVECs or HBMVECs to chemo-attract IMAC, an immortalized macrophage cell line in a modified Boyden chamber as above. Almost no transmigration of macrophages was observed in the case of siNT-conditioned media (Fig 6H; Fig S7C). Strikingly, siCCM2-conditioned media provoked a rapid transmigration of the macrophages suggesting that siCCM2 ECs had secreted chemo-attractive factors that siNT HUVECs had not (Fig 6H; Fig S7C). Importantly, this chemo-attraction was inhibited when ROCK2 but not ROCK1 was additionally silenced (Fig 6H; Fig S7C). Therefore, siCCM2 ECs secrete paracrine factors that can attract immune cells such as macrophages. Moreover, these chemo-attraction skills depend on ROCK2.

Overall, these results demonstrate for the first time to our knowledge that, when CCM2 is lost, ECs cultured *in vitro* undergo a SASP that is driven by the cytoskeletal and molecular disorders provoked by ROCKs dysfunctions. A major consequence of this SASP is a profound ROCKs-dependent remodelling of the microenvironment leading to the recruitment of wild-type ECs and immune cells.

Discussion

Many cellular pathways are dysregulated in CCM-deficient ECs and it has been difficult to propose a mechanistic model that could take into account all these aspects. In these cells, transition in cellular fate(18) upon morphological and cytoskeletal changes during the loss of cell-cell junctions(19,29,46) are associated with overproduction of ROS(16), decreased autophagy(17), secretion of metalloproteases(12–14) or cytokines(15) and increased integrin(19,20), p38(21), MEKK3/KLF2(20,22,23) and TLR4(24) signaling. The first breakthrough of this current study is to show, for the first time to our knowledge, that CCM2-deficient ECs engage *in vitro* towards a Senescence-Associated Secretory Phenotype (SASP) (Fig 7). Multiple senescent traits were validated such as a transcriptomic SASP signature (Fig 1D), high lysosomal SA- β -galactosidase activity, an upregulation of CDK inhibitors, a cell cycle blockage in G1 phase, the presence of SAHF along with the secretion of chemo-attractant factors (Fig 2). Moreover, we show that the functional consequence of this SASP is an acquired ability of CCM2-deficient ECs to invade the ECM and recruit wild-type ECs and immune cells (Fig 6 G-H). Whereas the absence of *in vivo* data is a limitation to our work, our studies on pure and mixed populations of CCM2-depleted and WT ECs have brought up new hypotheses on the mechanisms underlying the mosaicism of the CCM lesions by proposing the juxtacrine (Fig 6E) and paracrine (Fig 6F, G) attraction of WT ECs and immune cells by mutant ECs. These hypotheses will have to be tested *in vivo*.

The SASP is characterized by cell growth arrest, widespread changes in chromatin organization and gene expression(36). These changes also include the secretion of numerous pro-inflammatory cytokines, chemokines, growth factors and proteases(43). Acute senescence is beneficial in development, tissue regeneration or cancer through the clearance of senescent cells by the immune system(47). Chronic senescence triggers chronic inflammation that can on the contrary favour age-related diseases including cancer, fibrosis, cardiovascular diseases, type 2 diabetes, osteoarthritis or neurological disorders(33). Indeed, the long-term secreted pro-inflammatory factors promote cell proliferation, microenvironment remodelling, angiogenesis and inflammation in a paracrine manner. Remarkably, decreased autophagy(48), ROS overproduction(49), P38 MAPK(50), KLF2/4(51,52) and TLR4(53) signaling pathways have all been involved in the induction of the SASP either through regulation of CDK inhibitors or through the NF κ B or C/EBP β -driven expression of cytokines. Therefore, we propose that each of the dysregulated features of CCM-deficient ECs represents a different facet of the same cellular state. Future research should help reconstructing the complex chronology of the different events in the framework of this SASP. This could help identifying key therapeutic targets for either single or combinatorial drug treatments to block at their root the defective molecular pathways involved in the CCM2 disease. Senolytic drugs and drugs targeting the SASP *per se* are currently under pre-clinical trials for cancer therapy or other age-related diseases(33). They could be tested to prevent the formation and expansion of CCM lesions. A recent study strongly supports that premature aging of the neurovascular system could be the cause of CCM disease by showing that aging and CCM brains share common dysregulated features including impaired endothelial barrier function, inflammation, 320 DEGs, plasma molecules and imaging biomarkers (54).

A third hit corresponding to an oncogenic mutation on PI3K was recently detected in human CCM lesions that adds to the somatic loss-of-function mutation on the *CCM* genes (55). Interestingly, cellular senescence is a well-known response to oncogenic stress which arrests the aberrant proliferation of the cancerous cell(36). The expansion of ECs through several passages in our *in vitro* experiments may have mimicked the oncogenic stress occurring *in vivo*. Importantly, it has allowed the discovery of the increased sensitivity of KRIT- and CCM2-depleted ECs to senescence. Differently from KRIT and CCM2, the loss of CCM3 was actually shown to preserve primary ECs from replicative senescence *in vitro*(56). We found that CCM3 depletion does not at least increase the sensitivity of the ECs to replicative senescence (Fig 3). These differences in sensitivity to senescence may explain the different time courses of CCM diseases. Premature senescence of KRIT- or CCM2-deficient ECs after a first phase of clonal proliferation may lead to the progressive maturation of lesions through recruitment of WT ECs and to the late onset of the CCM1/2 disease. Differently, a more prolonged phase of clonal proliferation of CCM3-deficient ECs may trigger the formation of aggressive lesions at early age. Using the confetti reporter system in *Ccm1/2* mouse models made compatible with SA- β -galactosidase staining would help testing the occurrence of a SASP *in vivo*, its time course and allow the comparison with the *Ccm3* model.

The second major breakthrough of this study is that dysregulated ROCKs are involved in the onset of this SASP in our *in vitro* endothelial models. The fact that cellular mechanical defects can provoke senescence is an emerging area of investigations(57). We previously showed that upon the loss of CCM1/2, a vicious cycle sets up between aberrant ECM remodelling and increased intracellular contractility which breaks the permeability barrier of the endothelium(19). Moreover, we demonstrated that placing WT ECs on ECM remodelled by mutant ECs provoke CCM-like morphological defects in these cells(19). Going deeper into mechanistic investigations, we showed that upon the loss of CCM2, ROCK2 is delocalized from VE-cadherin junctions while ROCK1 gets over activated, enhancing the polymerization of β 1 integrin-anchored stress fibers(29). Here we uncover for the first time that, beyond their role in the disruption of the endothelial monolayer architecture, dysregulated ROCKs are instrumental in the *in vitro* transition of CCM2-depleted ECs towards a SASP (Fig 7).

ROCK2 controls the expression of a very significant fraction of the genes dysregulated upon the loss of CCM2 among which genes involved in senescence, cell cycle and paracrine SASP factors. The tendency to opposite expression profiles in absence of CCM2 or ROCK2 suggests that ROCK2 could gain a broad transcriptional regulatory function when its scaffold CCM2 is lost (Fig 4B). In fact, ROCK2 has already been involved in cellular senescence(58). In this study, the loss of the two ROCK isoforms led to senescence of MEF and was due to the downregulation of CDK1, CKS1 and cyclin2A. Intriguingly, we observe a similar downregulation of these genes in HUVECs when CCM2 is lost (Fig S3), but contrary to this other study, their expression is rescued by the additional silencing of ROCK2. This suggests that the presence or absence of CCM2 ~~has~~ could have a strong influence on the transcriptional activity of ROCK2. KRIT is found at cell-cell junctions and shuttles between the cytoplasm and the nucleus(59,60). We previously showed that it acts as a scaffold to recruit ROCK2 at

397 VE-cadherin dependent-Adherens junctions(29). ROCK2 has also been shown to translocate to
398 the nucleus(61,62). It is therefore possible that KRIT and ROCK2 shuttle together and that
399 KRIT loss impairs ROCK2 nuclear localization. Future mechanistic studies will be necessary
400 to understand whether and how ROCKs interplay with the CCM complex to modulate ROCK2
401 nucleocytoplasmic shuttling and its regulatory functions on gene expression.

402
403 We previously showed that ROCK1 overactivation allows CCM2-depleted HUVECs to exert
404 stronger traction forces on the ECM (19,29). Here we show that ROCK1 enables the
405 mechanosensitive degradation and invasion of the ECM by the senescent CCM2-depleted ECs
406 and by neighbouring WT ECs. Since ECs pull on their microenvironment to invade it(63), it is
407 likely that these stronger forces are responsible for enhanced invasion. Further investigations
408 will help to better understand the molecular events at play. Like ROCK2, ROCK1 affects gene
409 expression downstream of CCM2 though to a lesser extent. Moreover, inhibition of the myosin
410 motor or silencing of ROCK1 is enough to block senescence. These data suggest that cross talks
411 may exist between the contractility of the acto-myosin cytoskeleton and the transcription of
412 genes involved in SASP. Indeed, mechanosensitive transcription factors and/or epigenetic
413 factors could have their activity affected by the CCM/ROCKs-dependent increase in acto-
414 myosin contractility. As such, it is known that F-actin polymerization controls the shuttling of
415 MRTF to the nucleus and that ROCK2 is required for YAP nuclear localization (64,65).
416 Moreover, ROCK2 binds to and phosphorylates p300 increasing its acetyltransferase
417 activity(61). The mechanosensitive transcription factors KLF2 and KLF4 have a causative role
418 in the pathogenesis of the CCM disease(13,20,23). Intriguingly, KLF2/4 transcriptional
419 activities are modified by acetylation by p300(66,67) and the anti-inflammatory function of
420 KLF2 requires p300(66). The regulation of p300 by ROCK2 may control in turn KLF2/4 anti-
421 inflammatory activities. Future investigations should unravel how ROCK1 and ROCK2
422 cooperate to regulate chromatin organization and gene expression through the control of
423 mechanosensitive transcription machineries.

424
425 Overall, this study demonstrates that CCM2-deficient ECs undergo a SASP *in vitro* that is
426 driven by the cytoskeletal, transcriptional and molecular disorders provoked by ROCKs
427 dysfunctions. Remarkably, this discovery unifies all the known dysregulated traits of CCM1/2-
428 deficient ECs into a unique cellular state that could, if validated *in vivo*, trigger the remodelling
429 of a microenvironment favourable for the chronic recruitment of wild-type ECs and immune
430 cells to the site of the lesion. These *in vitro* observations open new avenues for mechanistic *in*
431 *vivo* studies on the dynamics and penetrance of the CCM disease as well as for exploring new
432 therapies.

Material and Methods

Cell culture and transfections:

Pooled HUVECs (human umbilical vein endothelial cells) and HBMVECs (human brain microvascular endothelial cells) were obtained from Lonza and Pellobiotech respectively. Upon reception, HUVECs at passage 0 and HBMVECs at passage 2 were expanded over 2 and 1 passage respectively in collagen 1 (from rat tail, BD) coated flasks in complete EGM-2 medium (HUVECs) or EGM-2MV (HBMVECs) supplemented with 100 U/ml penicillin and 100 µg/ml streptomycin at 37°C in a 5% CO₂ - 3% O₂ humidified chamber. Cells were transfected twice at 24 h-interval with 30 nM siRNA and Lipofectamine RNAi max (Life Technologies, ref. 13778-150) according to the manufacturer's instructions in 37°C in a regular 5% CO₂ in a humidified chamber. For double transfections, 30 nM of each siRNA duplexes (Dharmacon smartpool ON-TARGET plus Thermo Scientific) was used; Non-targeting siRNA #1, CCM2; ref. L-014728-01), KRIT; ref. L-003825-00, CCM3; ref. L-004436-00, ROCK1; ref. L-003536-00 and ROCK2; ref. L-004610-00. When required, Blebbistatin, Y-27632 and GM6001 were used at 10 µM final. IMAC (SV40 immortalized mouse bone marrow derived macrophages, gift from B. Py, CIRI, Lyon) were cultured in DMEM supplemented with 10% foetal calf serum, 100 U/ml penicillin and 100 µg/ml streptomycin at 37°C in a 5% CO₂.

RNA sequencing and differential analysis:

One million of siRNA transfected HUVECs were seeded at confluence the day after the second round of transfection in wells of 6-well plates coated with collagen 1 (from rat tail, BD) and cultured for 48h in complete media at 37°C, 5% CO₂. Three independent experiments were performed, each with 6 experimental conditions: siNT, siCCM2, siCCM2+siROCK1, siCCM2+siROCK2, siROCK1 and siROCK2. Total RNA were extracted from HUVECs using the NucleoSpin RNA II kit (Macherey-Nagel) according to the manufacturer's instructions. cDNA libraries were prepared with the TruSeq Stranded mRNA Sample Preparation (Illumina) and sequenced on a HiSeq 2500 Illumina platform using single-end 50 basepair reads at the MGX facility (Montpellier). Fastq files were aligned using STAR (2.5.2b) on UCSC hg19 genome. The contents of the annotation directories were downloaded from UCSC on: July 17, 2015. Bam files were counted using htseq-count (0.11.2.) with option -t exon -f bam -r pos -s reverse -m intersection-strict -nonunique none. Differential analyses were performed with SARTools (1.4.1) (68) using DESeq2 (1.12.3) (69) and default options. P-values were adjusted with Benjamini-Hochberg procedure(35) set for 5% of FDR. Heatmaps using a correlation matrix and boxplots were obtained with custom R script (3.3.0). The raw sequencing data used in this study are available in the National Center for Biotechnology Information's Gene Expression Omnibus (GEO) database and are accessible through GEO series accession number (pending).

Data Availability: The raw data (FastQ files) and processed data (count files) are deposited in the Gene Expression Omnibus database under ID code GEO: GSE165406, token gnujmwcdjohhkb (for reviewers). All data supporting the findings of this study are available from the corresponding author on reasonable request.

Bioinformatics analyses:

Gene ontology analyses on DEGs in siCCM2 condition (fold change [FC] ≥ 2 ; $P < 0.05$ with FDR corrected using Benjamini Horchberg method (35)) were made with PANTHER version 15,0 Released 2020-02-14 using slim cellular components and biological processes. Enriched pathways analyses were conducted with Reactome. DEGs ($P < 0.05$, 5% FDR) rescued by additional silencing of ROCK1 or ROCK2 were recovered at the union of Venn diagrams of DEGs in siCCM2 vs siNT and DEGs in siCCM2 vs siCCM2+ROCK1 or ROCK2 respectively. Gene Set Enrichment Analyses were conducted using GSEA software from Broad Institute, UC San Diego(70).

Quantitative RT-PCR:

Purified RNA (1 μ g) were reverse transcribed using the iScript Reverse Transcription Supermix (Biorad). Quantitative real-time PCR (Q-PCR) was performed with iTaq Universal SYBR Green Supermix (Biorad) in a 20 μ l reaction on a thermal cycler (C-1000 Touch; Bio-Rad Laboratories). Product sizes were controlled by DNA gel electrophoresis and the melt curves were evaluated using CFX Manager (Bio-Rad Laboratories). A total of three housekeeping genes were selected for their stability in HUVECs or HBMVECs under our experimental conditions, using the three analytical software programs, geNorm, Normfinder and Bestkeeper (71,72). We used the relative expression software tool CFX Manager for relative quantification, and normalization was achieved using a normalization factor from all reference genes(71). The mean of three technical replicates was calculated per biological replicate.

Immunofluorescence staining:

HUVECs or HBMVECs were seeded at 5×10^4 cells or 2×10^5 cells in 24-well plates on coverslips coated with 10 μ g/ml fibronectin (from human plasma, Sigma Aldrich) and incubated overnight in complete EBM-2 medium. Cells were fixed with 4% PFA, permeabilized with 0.2% Triton X-100, and incubated with anti-activated $\beta 1$ integrin clone 9EG7 ((BD Biosciences, 1/200), anti-Ki67 (AN9260 Millipore, 1/200), anti-HIRA (WC119, Millipore, 1/200) and anti β -catenin clone 8E7 (Merck, 1/2000). After rinsing, coverslips were incubated in Goat anti-Mouse or anti-Rabbit IgG (H+L) highly cross-adsorbed secondary antibody, Alexa Fluor conjugated AF 488, AF 546, AF 647 (Invitrogen, 1/1000) and phalloidin conjugates with Atto 647 (Sigma, 1/2000). The coverslips were mounted in Mowiol/DAPI solution and imaged on an epifluorescent Axiomager microscope (Zeiss) at 63X magnification.

SA-B-Galactosidase staining:

HUVECs or HBMVECs were seeded 48 hours after the second siRNA transfection at a density of 5×10^4 in 24-well plates coated with 10 μ g/mL fibronectin and incubated overnight in complete EBM-2-medium. Senescence-Associated β -galactosidase activity was assessed using a SA- β -galactosidase staining kit according to the manufacturer's instructions (Cell Signaling). Positive cells were counted manually out of more than 100 cells total.

BrdU assay:

HUVECs were seeded 48 hours after the second siRNA transfection at a density of 2×10^5 cells in 6-well plates coated with 100 μ g/mL collagen 1 and incubated overnight in complete EBM-2 medium. The BrdU assay was performed with the BD Accuri C6 flow cytometer using the APC-BrdU flow kit according to the manufacturer's instructions (Cell Signaling).

xCELLigence proliferation assay:

Proliferation assay was performed using the xCELLigence Real-Time Cell Analysis (RTCA) DP instrument in combination with E-plate 16 (ACEA Biosciences) coated with 100 μ L of 100 μ g/mL collagen 1 (from rat tail) for 30 min at 37°C and washed 2 times with PBS 1X. 40 μ L of complete EBM-2 medium was added and baseline without cells was made with RTCA software. SiRNA transfected HUVECs or HBMVECs were seeded at 5-10% confluence 48h after the second round of transfection in 100 μ L of complete EBM-2-medium. Impedance measurements were recorded every 5 min during 24h. Impedance was normalized at 4 hours after seeding to eliminate the contribution of cell spreading and adhesion to the signal. Slope measurement was performed between 4h and 24h.

Matrigel invasion assay:

This assay was performed using the xCELLigence RTCA DP instrument in combination with CIM-Plate 16 (ACEA Biosciences). A layer of 3.3% of growth factor reduced Matrigel (Corning) diluted with EBM basal media was poured on ice in the upper chamber and incubated overnight at 37°C for polymerization. 40 μ L basal EBM media was added to the upper chamber and the baseline made after equilibration at 37°C. After setting the baseline, 3×10^4 WT HUVECs were added to the upper chamber. The conditioned media from siRNA transfected cells was recovered 48 h after the second round of transfection and centrifuged at 12000 rpm for 5 min and 160 μ L was added to the lower chamber of the CIM-plate. After one hour of equilibration at 37°C, impedance was measured every 3 minutes for 24 hours.

Chemo-attraction assay:

This assay was performed using the xCELLigence Real-Time Cell Analysis (RTCA) DP instrument in combination with CIM-Plate 16 (ACEA Biosciences). After setting the baseline, 3×10^5 IMAC were added in 100 μ L of basal EBM in the upper chamber and 48h-conditioned media from siRNA transfected HUVECs or HBMVECs added to the lower chamber of the CIM-plate. After 30 min equilibration at 37°C, impedance was measured every 3 minutes for 24 hours.

Gelation degradation assay:

Coverslips in 24 well-plates were coated with gelatin-Alexa488 dye as previously described (73). SiRNA transfected HUVECs or HBMVECs were seeded 48h after the second siRNA transfection at 5×10^4 /well and incubated in OptiMEM medium overnight at 37°C in a 5% CO₂ incubator, fixed with 4% PFA, and washed with PBS twice. For a quantitative analysis of the degradative skill of siRNA transfected cells, 5 images per condition were acquired over the entire coverslip with an epifluorescent Axiomager microscope (Zeiss) at 40X magnification, and were converted to binary images using B&W thresholding on ImageJ. The total area of the

black zones corresponding to the total area of degradation of the fluorescent gelatin was measured.

3D-PEG invasion assays:

Poly-ethylene glycol (PEG) hydrogels were prepared on ice in EBM-2 complete media by combining an MMP-sensitive peptide modified PEG precursor (8-arm 40kDa,(74)) at 1.5% polymer concentration, 50 μ M Lys-RGD peptide (Pepmic), and 1 μ M sphingosine-1-phosphate (S1P, Sigma-Aldrich). The hydrogels were enzymatically crosslinked using a reconstituted and thrombin-activated Factor XIII (Fibrogammin, CSL Behring), prepared as previously described (75)) at 10% of total hydrogel volume. A 20 μ L volume of the hydrogel suspension was pipetted into a modified imaging chamber (Secure-Seal™ hybridization sealing systems, ThermoFisher Scientific) attached to the bottom of a 24-well plate held vertically (63). The hydrogel was allowed to polymerize for 30 minutes in this orientation at room temperature prior to cell seeding. Depending on the study, a confluent cell monolayer composed of either 5×10^4 siRNA transfected GFP-HUVECs or a 1:1 ratio mixture of siRNA transfected GFP-HUVECs and naïve RFP-HUVECs was allowed to adhere to the PEG meniscus at 37°C, 5% CO₂ for 1 hour and then placed back horizontally with 1mL of EBM-2 complete media. Fixation with 4% PFA in DPBS was performed after 24 hours. Sprouts invading the PEG hydrogel were imaged using a Leica SP8 inverted confocal microscope with an HC PL APO 10x, 0.4 numerical aperture dry objective to obtain image stacks at 1024x1024 pixels with a 50 μ m Z-stack at 1-1.5 μ m Z-spacing. A Z-projection of each image was used to manually quantify invasion distances using the line measurement tool of ImageJ. More than 100 sprouts were analyzed per technical replicate.

Statistical tests:

Results were assessed by the Tukey's multiple comparison tests post-ANOVA to compare with control; a 0.5 alpha level was used for all comparisons. Prism software was used to conduct the statistical analysis of all data. $P < 0.05$ was considered to be significant. * $P < 0.05$, ** $P < 0.05$, *** $P < 0.005$. n represents biological replicates.

Acknowledgements:

Most of the computations presented in this paper were performed using the CIMENT/GRICAD infrastructure (<https://gricad.univ-grenoble-alpes.fr>). The authors acknowledge the EpiMed core facility (<http://epimed.univ-grenoble-alpes.fr>) for their support and assistance in this work. This study was supported by the ANR (ANR-17-CE13-022), the Fondation pour la Recherche Médicale FRM (DEQ20170336702), the International Emerging Action CNRS, the association Espoir contre le Cancer Isère, the FWO project G087018N, infrastructure grant I009718N, Hercules Foundation (G0H6316N), the European Research Council under the European Union's Seventh Framework Program (FP7/2007–2013)/ ERC Grant Agreement No. 308223). PhD fellowship grants were supported by ANR and FRM to D.R.V. and FWO (1S68818N) to A.S. We would like to thank Claudia Röedel, Béatrice Eymin, and Gwénola Boulday for sharing ideas and reagents, Salim Seyfried for critical reading of the manuscript, and Christiane Oddou for excellent technical assistance.

Author contributions

D.R.V., A.S., H.V.O., E.F. conceived the project and designed experiments; D.R.V., A.S., S.M., E.P., E.F. performed experiments; F.C., D.R.V., E.F. analyzed the bioinformatical data; O.D. contributed to scientific discussion; P.R. provided reagents; C.A.R., E.F. and H.V.O. provided funding; E.F. wrote the manuscript which has been revised by all authors.

Figure legends:

Table S1: Level of expression of DEGs with $\log_2FC > 1$ ($P < 0.05$, FDR corrected using Benjamini Horchberg method) in the 6 different conditions of siRNA.

Table S2: Gene ontology analysis of DEGs in siCCM2 HUVECs with $\log_2FC > 1$ ($P < 0.05$, FDR corrected using Benjamini Horchberg method).

Table S3: Gene sets of Senescence and SASP used for GSEA analyses.

Table S4: Lists of DEGs with $\log_2FC > 1$ ($P < 0.05$, FDR corrected using Benjamini Horchberg method) in siCCM2 rescued by ROCKs.

Table S5: Gene Ontology Analysis on DEGs with $\log_2FC > 1$ rescued by ROCKs.

Table S6: Cytokines upregulated with $FC > 2$ in siCCM2 HUVECs and their biological effects on immune and endothelial cells.

References

1. Clatterbuck RE, Eberhart CG, Crain BJ, Rigamonti D. Ultrastructural and immunocytochemical evidence that an incompetent blood-brain barrier is related to the pathophysiology of cavernous malformations. *J Neurol Neurosurg Psychiatry* [Internet]. 2001 Aug [cited 2016 Apr 4];71(2):188–92. Available from: <http://www.ncbi.nlm.nih.gov/pubmed/11459890>
2. Labauge P, Denier C, Bergametti F, Tournier-Lasserre E. Genetics of cavernous angiomas. *Lancet Neurol* [Internet]. 2007 Mar [cited 2016 Apr 28];6(3):237–44. Available from: <http://www.ncbi.nlm.nih.gov/pubmed/17303530>
3. Awad IA, Polster SP. Cavernous angiomas: deconstructing a neurosurgical disease. *J Neurosurg* [Internet]. 2019 Jul 1 [cited 2019 Sep 15];131(1):1–13. Available from: <http://www.ncbi.nlm.nih.gov/pubmed/31261134>
4. Riant F, Bergametti F, Fournier HD, Chapon F, Michalak-Provost S, Cecillon M, et al. CCM3 mutations are associated with early-onset cerebral hemorrhage and multiple meningiomas. *Mol Syndromol* [Internet]. 2013 Apr [cited 2020 Jun 30];4(4):165–72. Available from: [/pmc/articles/PMC3666455/?report=abstract](http://pmc/articles/PMC3666455/?report=abstract)
5. Shenkar R, Shi C, Rebeiz T, Stockton RA, McDonald DA, Mikati AG, et al. Exceptional aggressiveness of cerebral cavernous malformation disease associated with PDCD10 mutations. *Genet Med* [Internet]. 2015 Mar 14 [cited 2017 Jun 1];17(3):188–96. Available from: <http://www.ncbi.nlm.nih.gov/pubmed/25122144>
6. Labauge P, Brunereau L, Lévy C, Laberge S, Houtteville JP. The natural history of familial cerebral cavernomas: A retrospective MRI study of 40 patients. *Neuroradiology* [Internet]. 2000 [cited 2020 Jun 30];42(5):327–32. Available from: <https://pubmed-ncbi-nlm-nih-gov.proxy.insermbiblio.inist.fr/10872151/>
7. McDonald DA, Shenkar R, Shi C, Stockton RA, Akers AL, Kucherlapati MH, et al. A novel mouse model of cerebral cavernous malformations based on the two-hit mutation hypothesis recapitulates the human disease. *Hum Mol Genet* [Internet]. 2011;20(2):211–22. Available from: http://www.ncbi.nlm.nih.gov/entrez/query.fcgi?cmd=Retrieve&db=PubMed&dopt=Citation&list_uids=20940147
8. Pagenstecher A, Stahl S, Sure U, Felbor U. A two-hit mechanism causes cerebral cavernous malformations: Complete inactivation of CCM1, CCM2 or CCM3 in affected endothelial cells. *Hum Mol Genet* [Internet]. 2009 [cited 2020 Dec 17];18(5):911–8. Available from: <https://pubmed-ncbi-nlm-nih-gov.insb.bib.cnrs.fr/19088124/>
9. Rath M, Pagenstecher A, Hoischen A, Felbor U. Postzygotic mosaicism in cerebral cavernous malformation. *J Med Genet*. 2020 Mar 1;57(3):212–6.
10. Detter MR, Snellings DA, Marchuk DA. Cerebral cavernous malformations develop through clonal expansion of mutant endothelial cells. *Circ Res* [Internet]. 2018 [cited 2020 Jun 30];123(10):1143–51. Available from: <https://pubmed-ncbi-nlm-nih-gov.proxy.insermbiblio.inist.fr/30359189/>
11. Malinverno M, Maderna C, Abu Taha A, Corada M, Orsenigo F, Valentino M, et al.

- Endothelial cell clonal expansion in the development of cerebral cavernous malformations. *Nat Commun* [Internet]. 2019 Dec 24 [cited 2019 Jul 16];10(1):2761. Available from: <http://www.ncbi.nlm.nih.gov/pubmed/31235698>
12. Bicer A, Guclu B, Ozkan A, Kurtkaya O, Koc DY, Necmettin Pamir M, et al. Expressions of angiogenesis associated matrix metalloproteinases and extracellular matrix proteins in cerebral vascular malformations. *J Clin Neurosci* [Internet]. 2010 Feb [cited 2020 Jun 30];17(2):232–6. Available from: <https://pubmed-ncbi-nlm-nih-gov.proxy.insermbiblio.inist.fr/20036554/>
13. Zhou Z, Tang AT, Wong W-Y, Bamezai S, Goddard LM, Shenkar R, et al. Cerebral cavernous malformations arise from endothelial gain of MEKK3-KLF2/4 signalling. *Nature* [Internet]. 2016 Apr 7 [cited 2016 May 11];532(7597):122–6. Available from: <http://www.ncbi.nlm.nih.gov/pubmed/27027284>
14. Fujimura M, Watanabe M, Shimizu H, Tominaga T. Expression of matrix metalloproteinases (MMPs) and tissue inhibitor of metalloproteinase (TIMP) in cerebral cavernous malformations: Immunohistochemical analysis of MMP-2, -9 and TIMP-2. *Acta Neurochir (Wien)* [Internet]. 2007 Feb [cited 2020 Jul 1];149(2):179–83. Available from: <https://pubmed-ncbi-nlm-nih-gov.insb.bib.cnrs.fr/17043747/>
15. Noshiro S, Mikami T, Kataoka-Sasaki Y, Sasaki M, Ohnishi H, Ohtaki S, et al. Co-expression of tissue factor and IL-6 in immature endothelial cells of cerebral cavernous malformations. *J Clin Neurosci* [Internet]. 2017 Mar 1 [cited 2020 Jun 30];37:83–90. Available from: <https://pubmed-ncbi-nlm-nih-gov.proxy.insermbiblio.inist.fr/28087183/>
16. Goitre L, Balzac F, Degani S, Degan P, Marchi S, Pinton P, et al. KRIT1 regulates the homeostasis of intracellular reactive oxygen species. *PLoS One* [Internet]. 2010 [cited 2020 Jun 30];5(7):1–22. Available from: <https://pubmed-ncbi-nlm-nih-gov.insb.bib.cnrs.fr/20668652/>
17. Marchi S, Corricelli M, Trapani E, Bravi L, Pittaro A, Delle Monache S, et al. Defective autophagy is a key feature of cerebral cavernous malformations. *EMBO Mol Med* [Internet]. 2015 Nov [cited 2020 Jun 30];7(11):1403–17. Available from: <https://pubmed-ncbi-nlm-nih-gov.insb.bib.cnrs.fr/26417067/>
18. Maddaluno L, Rudini N, Cuttano R, Bravi L, Giampietro C, Corada M, et al. EndMT contributes to the onset and progression of cerebral cavernous malformations. *Nature* [Internet]. 2013 Jun 9 [cited 2017 Mar 27];498(7455):492–6. Available from: <http://www.ncbi.nlm.nih.gov/pubmed/23748444>
19. Faurobert E, Rome C, Lisowska J, Manet-Dupé S, Boulday G, Malbouyres M, et al. CCM1-ICAP-1 complex controls β 1 integrin-dependent endothelial contractility and fibronectin remodeling. *J Cell Biol* [Internet]. 2013/08/07. 2013;202(3):545–61. Available from: <http://www.ncbi.nlm.nih.gov/pubmed/23918940>
20. Renz M, Otten C, Faurobert E, Rudolph F, Zhu Y, Boulday G, et al. Regulation of β 1 Integrin-Klf2-Mediated Angiogenesis by CCM Proteins. *Dev Cell*. 2015;32(2).
21. Uhlik MT, Abell AN, Johnson NL, Sun W, Cuevas BD, Lobel-Rice KE, et al. Rac-MEKK3-MKK3 scaffolding for p38 MAPK activation during hyperosmotic shock. *Nat Cell Biol* [Internet]. 2003 Dec [cited 2016 Apr 9];5(12):1104–10. Available from:

697 <http://www.ncbi.nlm.nih.gov/pubmed/14634666>

698 22. Zhou Z, Rawnsley DR, Goddard LM, Pan W, Cao X-J, Jakus Z, et al. The Cerebral
699 Cavernous Malformation Pathway Controls Cardiac Development via Regulation of
700 Endocardial MEKK3 Signaling and KLF Expression. *Dev Cell* [Internet]. 2015 Jan 26
701 [cited 2017 Sep 6];32(2):168–80. Available from:
702 <http://www.ncbi.nlm.nih.gov/pubmed/25625206>

703 23. Cuttano R, Rudini N, Bravi L, Corada M, Giampietro C, Papa E, et al. KLF4 is a key
704 determinant in the development and progression of cerebral cavernous malformations.
705 *EMBO Mol Med* [Internet]. 2016 Jan 1 [cited 2017 Mar 27];8(1):6–24. Available from:
706 <http://www.ncbi.nlm.nih.gov/pubmed/26612856>

707 24. Tang AT, Choi JP, Kotzin JJ, Yang Y, Hong CC, Hobson N, et al. Endothelial TLR4
708 and the microbiome drive cerebral cavernous malformations. *Nature* [Internet]. 2017
709 May 10 [cited 2017 May 23];545(7654):305–10. Available from:
710 <http://www.ncbi.nlm.nih.gov/pubmed/28489816>

711 25. Li J, Zhao Y, Coleman P, Chen J, Ting KK, Choi JP, et al. Low fluid shear stress
712 conditions contribute to activation of cerebral cavernous malformation signalling
713 pathways. *Biochim Biophys Acta - Mol Basis Dis* [Internet]. 2019 Nov 29 [cited 2019
714 Aug 27];1865(11):165519. Available from:
715 <http://www.ncbi.nlm.nih.gov/pubmed/31369819>

716 26. Whitehead KJ, Chan AC, Navankasattusas S, Koh W, London NR, Ling J, et al. The
717 cerebral cavernous malformation signaling pathway promotes vascular integrity via
718 Rho GTPases. *Nat Med* [Internet]. 2009;15(2):177–84. Available from:
719 [http://www.ncbi.nlm.nih.gov/entrez/query.fcgi?cmd=Retrieve&db=PubMed&dopt=Cit](http://www.ncbi.nlm.nih.gov/entrez/query.fcgi?cmd=Retrieve&db=PubMed&dopt=Citation&list_uids=19151728)
720 [ation&list_uids=19151728](http://www.ncbi.nlm.nih.gov/entrez/query.fcgi?cmd=Retrieve&db=PubMed&dopt=Citation&list_uids=19151728)

721 27. Borikova AL, Dibble CF, Sciaky N, Welch CM, Abell AN, Bencharit S, et al. Rho
722 kinase inhibition rescues the endothelial cell cerebral cavernous malformation
723 phenotype. *J Biol Chem* [Internet]. 2010;285(16):11760–4. Available from:
724 [http://www.ncbi.nlm.nih.gov/entrez/query.fcgi?cmd=Retrieve&db=PubMed&dopt=Cit](http://www.ncbi.nlm.nih.gov/entrez/query.fcgi?cmd=Retrieve&db=PubMed&dopt=Citation&list_uids=20181950)
725 [ation&list_uids=20181950](http://www.ncbi.nlm.nih.gov/entrez/query.fcgi?cmd=Retrieve&db=PubMed&dopt=Citation&list_uids=20181950)

726 28. Stockton RA, Shenkar R, Awad IA, Ginsberg MH. Cerebral cavernous malformations
727 proteins inhibit Rho kinase to stabilize vascular integrity. *J Exp Med* [Internet].
728 2010;207(4):881–96. Available from:
729 [http://www.ncbi.nlm.nih.gov/entrez/query.fcgi?cmd=Retrieve&db=PubMed&dopt=Cit](http://www.ncbi.nlm.nih.gov/entrez/query.fcgi?cmd=Retrieve&db=PubMed&dopt=Citation&list_uids=20308363)
730 [ation&list_uids=20308363](http://www.ncbi.nlm.nih.gov/entrez/query.fcgi?cmd=Retrieve&db=PubMed&dopt=Citation&list_uids=20308363)

731 29. Lisowska J, Rödel CJ, Manet S, Miroshnikova YA, Boyault C, Planus E, et al. The
732 CCM1–CCM2 complex controls complementary functions of ROCK1 and ROCK2
733 that are required for endothelial integrity. *J Cell Sci* [Internet]. 2018 Aug 1 [cited 2018
734 Oct 9];131(15):jcs216093. Available from:
735 <http://www.ncbi.nlm.nih.gov/pubmed/30030370>

736 30. McDonald DA, Shi C, Shenkar R, Stockton RA, Liu F, Ginsberg MH, et al. Fasudil
737 decreases lesion burden in a murine model of cerebral cavernous malformation disease.
738 *Stroke* [Internet]. 2011/10/29. 2012;43(2):571–4. Available from:
739 <http://www.ncbi.nlm.nih.gov/pubmed/22034008>

- 740 31. Shenkar R, Shi C, Austin C, Moore T, Lightle R, Cao Y, et al. RhoA Kinase Inhibition
741 With Fasudil Versus Simvastatin in Murine Models of Cerebral Cavernous
742 Malformations. *Stroke* [Internet]. 2017 Jan [cited 2016 Dec 31];48(1):187–94.
743 Available from: <http://www.ncbi.nlm.nih.gov/pubmed/27879448>
- 744 32. Polster SP, Stadnik A, Akers AL, Cao Y, Christoforidis GA, Fam MD, et al.
745 Atorvastatin Treatment of Cavernous Angiomas with Symptomatic Hemorrhage
746 Exploratory Proof of Concept (AT CASH EPOC) Trial. *Neurosurgery* [Internet]. 2019
747 [cited 2020 Apr 24];85(6):843–53. Available from:
748 <http://www.ncbi.nlm.nih.gov/pubmed/30476251>
- 749 33. Paez-Ribes M, González-Gualda E, Doherty GJ, Muñoz-Espín D. Targeting senescent
750 cells in translational medicine. *EMBO Mol Med* [Internet]. 2019 Dec [cited 2020 Jun
751 30];11(12). Available from: [https://pubmed-ncbi-nlm-nih-](https://pubmed-ncbi-nlm-nih-gov.proxy.insermbiblio.inist.fr/31746100/)
752 [gov.proxy.insermbiblio.inist.fr/31746100/](https://pubmed-ncbi-nlm-nih-gov.proxy.insermbiblio.inist.fr/31746100/)
- 753 34. Zawistowski JS, Stalheim L, Uhlik MT, Abell AN, Ancrile BB, Johnson GL, et al.
754 CCM1 and CCM2 protein interactions in cell signaling: implications for cerebral
755 cavernous malformations pathogenesis. *Hum Mol Genet* [Internet]. 2005;14(17):2521–
756 31. Available from:
757 [http://www.ncbi.nlm.nih.gov/entrez/query.fcgi?cmd=Retrieve&db=PubMed&dopt=Cit](http://www.ncbi.nlm.nih.gov/entrez/query.fcgi?cmd=Retrieve&db=PubMed&dopt=Citation&list_uids=16037064)
758 [ation&list_uids=16037064](http://www.ncbi.nlm.nih.gov/entrez/query.fcgi?cmd=Retrieve&db=PubMed&dopt=Citation&list_uids=16037064)
- 759 35. Benjamini Y, Hochberg Y. Controlling the False Discovery Rate: A Practical and
760 Powerful Approach to Multiple Testing. *J R Stat Soc Ser B*. 1995 Jan;57(1):289–300.
- 761 36. Campisi J. Aging, Cellular Senescence, and Cancer. *Annu Rev Physiol* [Internet]. 2013
762 Feb 10 [cited 2020 Jun 30];75(1):685–705. Available from: [https://pubmed-ncbi-nlm-](https://pubmed-ncbi-nlm-nih-gov.proxy.insermbiblio.inist.fr/23140366/)
763 [nih-gov.proxy.insermbiblio.inist.fr/23140366/](https://pubmed-ncbi-nlm-nih-gov.proxy.insermbiblio.inist.fr/23140366/)
- 764 37. Hernandez-Segura A, de Jong T V, Melov S, Guryev V, Campisi J, Demaria M.
765 Unmasking Transcriptional Heterogeneity in Senescent Cells. *Curr Biol* [Internet].
766 2017 Sep 11 [cited 2019 Nov 7];27(17):2652–2660.e4. Available from:
767 <http://www.ncbi.nlm.nih.gov/pubmed/28844647>
- 768 38. Casella G, Munk R, Kim KM, Piao Y, De S, Abdelmohsen K, et al. Transcriptome
769 signature of cellular senescence. *Nucleic Acids Res* [Internet]. 2019 Oct 15 [cited 2019
770 Nov 7]; Available from: [https://academic.oup.com/nar/advance-](https://academic.oup.com/nar/advance-article/doi/10.1093/nar/gkz879/5587628)
771 [article/doi/10.1093/nar/gkz879/5587628](https://academic.oup.com/nar/advance-article/doi/10.1093/nar/gkz879/5587628)
- 772 39. De Cecco M, Ito T, Petrashen AP, Elias AE, Skvir NJ, Criscione SW, et al. L1 drives
773 IFN in senescent cells and promotes age-associated inflammation. *Nature* [Internet].
774 2019 Feb 7 [cited 2020 Jun 30];566(7742):73–8. Available from: [https://pubmed-ncbi-](https://pubmed-ncbi-nlm-nih-gov.insb.bib.cnrs.fr/30728521/)
775 [nlm-nih-gov.insb.bib.cnrs.fr/30728521/](https://pubmed-ncbi-nlm-nih-gov.insb.bib.cnrs.fr/30728521/)
- 776 40. Ly DH, Lockhart DJ, Lerner RA, Schultz PG. Mitotic misregulation and human aging.
777 *Science* (80-) [Internet]. 2000 Mar 31 [cited 2021 Jan 6];287(5462):2486–92.
778 Available from: <https://pubmed-ncbi-nlm-nih-gov.insb.bib.cnrs.fr/10741968/>
- 779 41. Matjusaitis M, Chin G, Sarnoski EA, Stolzing A. Biomarkers to identify and isolate
780 senescent cells [Internet]. Vol. 29, Ageing Research Reviews. Elsevier Ireland Ltd;
781 2016 [cited 2020 Jun 30]. p. 1–12. Available from: [https://pubmed-ncbi-nlm-nih-](https://pubmed-ncbi-nlm-nih-gov.insb.bib.cnrs.fr/27212009/)
782 [gov.insb.bib.cnrs.fr/27212009/](https://pubmed-ncbi-nlm-nih-gov.insb.bib.cnrs.fr/27212009/)

- 783 42. Faget D V., Ren Q, Stewart SA. Unmasking senescence: context-dependent effects of
784 SASP in cancer [Internet]. Vol. 19, *Nature Reviews Cancer*. Nature Publishing Group;
785 2019 [cited 2020 Jun 30]. p. 439–53. Available from: [https://pubmed-ncbi-nlm-nih-](https://pubmed-ncbi-nlm-nih-gov.proxy.insermbiblio.inist.fr/31235879/)
786 [gov.proxy.insermbiblio.inist.fr/31235879/](https://pubmed-ncbi-nlm-nih-gov.proxy.insermbiblio.inist.fr/31235879/)
- 787 43. Coppé J-P, Desprez P-Y, Krtolica A, Campisi J. The Senescence-Associated Secretory
788 Phenotype: The Dark Side of Tumor Suppression. *Annu Rev Pathol Mech Dis*
789 [Internet]. 2010 Jan [cited 2019 Jan 5];5(1):99–118. Available from:
790 <http://www.ncbi.nlm.nih.gov/pubmed/20078217>
- 791 44. Chan AC, Drakos SG, Ruiz OE, Smith AC, Gibson CC, Ling J, et al. Mutations in 2
792 distinct genetic pathways result in cerebral cavernous malformations in mice. *J Clin*
793 *Invest* [Internet]. 2011;121(5):1871–81. Available from:
794 [http://www.ncbi.nlm.nih.gov/entrez/query.fcgi?cmd=Retrieve&db=PubMed&dopt=Cit](http://www.ncbi.nlm.nih.gov/entrez/query.fcgi?cmd=Retrieve&db=PubMed&dopt= Citation&list_uids=21490399)
795 [ation&list_uids=21490399](http://www.ncbi.nlm.nih.gov/entrez/query.fcgi?cmd=Retrieve&db=PubMed&dopt= Citation&list_uids=21490399)
- 796 45. Shi C, Shenkar R, Du H, Duckworth E, Raja H, Batjer HH, et al. Immune Response in
797 Human Cerebral Cavernous Malformations. *Stroke* [Internet]. 2009 May 1 [cited 2021
798 Jan 7];40(5):1659–65. Available from: [https://pubmed-ncbi-nlm-nih-](https://pubmed-ncbi-nlm-nih-gov.insb.bib.cnrs.fr/19286587/)
799 [gov.insb.bib.cnrs.fr/19286587/](https://pubmed-ncbi-nlm-nih-gov.insb.bib.cnrs.fr/19286587/)
- 800 46. Lampugnani MG, Orsenigo F, Rudini N, Maddaluno L, Boulday G, Chapon F, et al.
801 CCM1 regulates vascular-lumen organization by inducing endothelial polarity. *J Cell*
802 *Sci* [Internet]. 2010;123(Pt 7):1073–80. Available from:
803 [http://www.ncbi.nlm.nih.gov/entrez/query.fcgi?cmd=Retrieve&db=PubMed&dopt=Cit](http://www.ncbi.nlm.nih.gov/entrez/query.fcgi?cmd=Retrieve&db=PubMed&dopt= Citation&list_uids=20332120)
804 [ation&list_uids=20332120](http://www.ncbi.nlm.nih.gov/entrez/query.fcgi?cmd=Retrieve&db=PubMed&dopt= Citation&list_uids=20332120)
- 805 47. Rhinn M, Ritschka B, Keyes WM. Cellular senescence in development, regeneration
806 and disease. *Dev* [Internet]. 2019 [cited 2020 Jul 1];146(20). Available from:
807 <https://pubmed-ncbi-nlm-nih-gov.proxy.insermbiblio.inist.fr/31575608/>
- 808 48. Cheon SY, Kim H, Rubinsztein DC, Lee JE. Autophagy, cellular aging and age-related
809 human diseases [Internet]. Vol. 28, *Experimental Neurobiology*. Korean Society for
810 Neurodegenerative Disease; 2019 [cited 2020 Jul 1]. p. 643–57. Available from:
811 <https://pubmed-ncbi-nlm-nih-gov.insb.bib.cnrs.fr/31902153/>
- 812 49. Salazar G. NADPH oxidases and mitochondria in vascular senescence [Internet]. Vol.
813 19, *International Journal of Molecular Sciences*. MDPI AG; 2018 [cited 2020 Jul 1].
814 Available from: <https://pubmed-ncbi-nlm-nih-gov.insb.bib.cnrs.fr/29710840/>
- 815 50. Freund A, Patil CK, Campisi J. p38MAPK is a novel DNA damage response-
816 independent regulator of the senescence-associated secretory phenotype. *EMBO J*
817 [Internet]. 2011 Apr 20 [cited 2020 Jul 1];30(8):1536–48. Available from:
818 <http://emboj.embopress.org/cgi/doi/10.1038/emboj.2011.69>
- 819 51. Yuedi D, Houbao L, Pinxiang L, Hui W, Min T, Dexiang Z. KLF2 induces the
820 senescence of pancreatic cancer cells by cooperating with FOXO4 to upregulate p21.
821 *Exp Cell Res* [Internet]. 2020 Mar 1 [cited 2020 Jun 26];388(1). Available from:
822 <https://pubmed-ncbi-nlm-nih-gov.proxy.insermbiblio.inist.fr/31866399/>
- 823 52. Xu Q, Liu M, Zhang J, Xue L, Zhang G, Hu C, et al. Overexpression of KLF4
824 promotes cell senescence through microRNA-203-survivin-p21 pathway. *Oncotarget*
825 [Internet]. 2016 [cited 2020 Jun 26];7(37):60290–302. Available from: <https://pubmed->

ncbi-nlm-nih-gov.proxy.insermbiblio.inist.fr/27531889/

53. Balistreri CR, Ruvolo G, Lio D, Madonna R. Toll-like receptor-4 signaling pathway in aorta aging and diseases: “its double nature” [Internet]. Vol. 110, *Journal of Molecular and Cellular Cardiology*. Academic Press; 2017 [cited 2020 Jul 1]. p. 38–53. Available from: <https://pubmed-ncbi-nlm-nih-gov.proxy.insermbiblio.inist.fr/28668304/>
54. Koskimäki J, Polster SP, Li Y, Romanos S, Srinath A, Zhang D, et al. Common transcriptome, plasma molecules, and imaging signatures in the aging brain and a Mendelian neurovascular disease, cerebral cavernous malformation. *GeroScience* [Internet]. 2020 Jun 17 [cited 2020 Jun 30]; Available from: <https://pubmed-ncbi-nlm-nih-gov.proxy.insermbiblio.inist.fr/32556941/>
55. Ren AA, Snellings DA, Su YS, Hong CC, Castro M, Tang AT, et al. PIK3CA and CCM mutations fuel cavernomas through a cancer-like mechanism. *Nature* [Internet]. 2021 Jun 10 [cited 2021 Jul 4];594(7862):271–6. Available from: <https://pubmed-ncbi-nlm-nih-gov.insb.bib.cnrs.fr/33910229/>
56. Guerrero A, Iglesias C, Raguz S, Floridia E, Gil J, Pombo CM, et al. The cerebral cavernous malformation 3 gene is necessary for senescence induction. *Aging Cell* [Internet]. 2015 Apr 1 [cited 2020 Jul 1];14(2):274–83. Available from: <https://pubmed-ncbi-nlm-nih-gov.proxy.insermbiblio.inist.fr/25655101/>
57. Gilbert HTJ, Swift J. The consequences of ageing, progeroid syndromes and cellular senescence on mechanotransduction and the nucleus [Internet]. Vol. 378, *Experimental Cell Research*. Elsevier Inc.; 2019 [cited 2021 Jun 24]. p. 98–103. Available from: <https://pubmed.ncbi.nlm.nih.gov/30836065/>
58. Kümper S, Mardakheh FK, McCarthy A, Yeo M, Stamp GW, Paul A, et al. Rho-associated kinase (ROCK) function is essential for cell cycle progression, senescence and tumorigenesis. *Elife* [Internet]. 2016 Jan 14 [cited 2020 Dec 17];5. Available from: <https://pubmed-ncbi-nlm-nih-gov.insb.bib.cnrs.fr/26765561/>
59. Zhang J, Rigamonti D, Dietz HC, Clatterbuck RE. Interaction between krit1 and malcavernin: Implications for the pathogenesis of cerebral cavernous malformations. *Neurosurgery* [Internet]. 2007 Feb [cited 2021 Jun 24];60(2):353–9. Available from: <https://pubmed-ncbi-nlm-nih-gov.insb.bib.cnrs.fr/17290187/>
60. Glading A, Han J, Stockton RA, Ginsberg MH. KRIT-1/CCM1 is a Rap1 effector that regulates endothelial cell cell junctions. *J Cell Biol* [Internet]. 2007;179(2):247–54. Available from: http://www.ncbi.nlm.nih.gov/entrez/query.fcgi?cmd=Retrieve&db=PubMed&dopt= Citation&list_uids=17954608
61. Tanaka T, Nishimura D, Wu R-C, Amano M, Iso T, Kedes L, et al. Nuclear Rho kinase, ROCK2, targets p300 acetyltransferase. *J Biol Chem* [Internet]. 2006 Jun 2 [cited 2019 Jan 5];281(22):15320–9. Available from: <http://www.jbc.org/lookup/doi/10.1074/jbc.M510954200>
62. Chen W, Nyuydzefe MS, Weiss JM, Zhang J, Waksal SD, Zanin-Zhorov A. ROCK2, but not ROCK1 interacts with phosphorylated STAT3 and co-occupies TH17/TFH gene promoters in TH17-activated human T cells. *Sci Rep* [Internet]. 2018 Dec 1 [cited 2021 Apr 8];8(1). Available from: <https://pubmed-ncbi-nlm-nih->

869 gov.proxy.insermbiblio.inist.fr/30413785/

870 63. Vaeyens MM, Jorge-Peñas A, Barrasa-Fano J, Steuwe C, Heck T, Carmeliet P, et al.
871 Matrix deformations around angiogenic sprouts correlate to sprout dynamics and
872 suggest pulling activity. *Angiogenesis*. 2020;

873 64. Finch-Edmondson M, Sudol M. Framework to function: Mechanosensitive regulators
874 of gene transcription [Internet]. Vol. 21, Cellular and Molecular Biology Letters.
875 BioMed Central Ltd.; 2016 [cited 2020 Jul 1]. Available from: [https://pubmed-ncbi-](https://pubmed-ncbi-nlm-nih.gov.proxy.insermbiblio.inist.fr/28536630/)
876 [nml-nih.gov.proxy.insermbiblio.inist.fr/28536630/](https://pubmed-ncbi-nlm-nih.gov.proxy.insermbiblio.inist.fr/28536630/)

877 65. Torrino S, Roustan F, Kaminski L, Bertero T, Pisano S, Ambrosetti D, et al. UBTD1 is
878 a mechano-regulator controlling cancer aggressiveness. *EMBO Rep* [Internet]. 2019
879 Apr [cited 2021 Apr 7];20(4). Available from: [https://pubmed-ncbi-nlm-nih-](https://pubmed-ncbi-nlm-nih-gov.proxy.insermbiblio.inist.fr/30804013/)
880 [gov.proxy.insermbiblio.inist.fr/30804013/](https://pubmed-ncbi-nlm-nih-gov.proxy.insermbiblio.inist.fr/30804013/)

881 66. SenBanerjee S, Lin Z, Atkins GB, Greif DM, Rao RM, Kumar A, et al. KLF2 is a
882 novel transcriptional regulator of endothelial proinflammatory activation. *J Exp Med*.
883 2004 May 17;199(10):1305–15.

884 67. Jia Z min, Ai X, Teng J fei, Wang Y peng, Wang B jun, Zhang X. p21 and CK2
885 interaction-mediated HDAC2 phosphorylation modulates KLF4 acetylation to regulate
886 bladder cancer cell proliferation. *Tumor Biol* [Internet]. 2016 Jun 1 [cited 2021 Apr
887 7];37(6):8293–304. Available from: <https://pubmed.ncbi.nlm.nih.gov/26729194/>

888 68. Varet H, Brillet-Guéguen L, Coppée JY, Dillies MA. SARTools: A DESeq2- and
889 edgeR-based R pipeline for comprehensive differential analysis of RNA-Seq data.
890 *PLoS One* [Internet]. 2016 Jun 1 [cited 2020 Jul 2];11(6). Available from:
891 <https://pubmed-ncbi-nlm-nih-gov.proxy.insermbiblio.inist.fr/27280887/>

892 69. Love MI, Huber W, Anders S. Moderated estimation of fold change and dispersion for
893 RNA-seq data with DESeq2. *Genome Biol* [Internet]. 2014 Dec 5 [cited 2020 Jul
894 2];15(12). Available from: <https://pubmed-ncbi-nlm-nih-gov.insb.bib.cnrs.fr/25516281/>

895 70. Subramanian A, Tamayo P, Mootha VK, Mukherjee S, Ebert BL, Gillette MA, et al.
896 Gene set enrichment analysis: A knowledge-based approach for interpreting genome-
897 wide expression profiles. *Proc Natl Acad Sci U S A* [Internet]. 2005 Oct 25 [cited 2020
898 Jul 2];102(43):15545–50. Available from: [https://pubmed-ncbi-nlm-nih-](https://pubmed-ncbi-nlm-nih-gov.proxy.insermbiblio.inist.fr/16199517/)
899 [gov.proxy.insermbiblio.inist.fr/16199517/](https://pubmed-ncbi-nlm-nih-gov.proxy.insermbiblio.inist.fr/16199517/)

900 71. Pfaffl MW, Tichopad A, Prgomet C, Neuvians TP. Determination of stable
901 housekeeping genes, differentially regulated target genes and sample integrity:
902 BestKeeper--Excel-based tool using pair-wise correlations. *Biotechnol Lett* [Internet].
903 2004 Mar [cited 2016 Apr 29];26(6):509–15. Available from:
904 <http://www.ncbi.nlm.nih.gov/pubmed/15127793>

905 72. Vandesompele J, De Preter K, Pattyn F, Poppe B, Van Roy N, De Paepe A, et al.
906 Accurate normalization of real-time quantitative RT-PCR data by geometric averaging
907 of multiple internal control genes. *Genome Biol* [Internet]. 2002 Jun 18 [cited 2016
908 Apr 29];3(7):RESEARCH0034. Available from:
909 <http://www.ncbi.nlm.nih.gov/pubmed/12184808>

910 73. Sharma VP, Entenberg D, Condeelis J. High-resolution live-cell imaging and time-

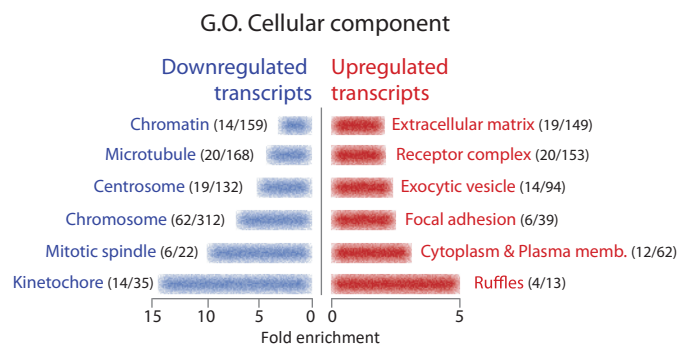
911 lapse microscopy of invadopodium dynamics and tracking analysis. *Methods Mol Biol*
912 [Internet]. 2013 [cited 2020 Jul 2];1046:343–57. Available from: [https://pubmed.ncbi-](https://pubmed.ncbi.nlm-nih-gov.proxy.insermbiblio.inist.fr/23868599/)
913 [nlm-nih-gov.proxy.insermbiblio.inist.fr/23868599/](https://pubmed.ncbi.nlm-nih-gov.proxy.insermbiblio.inist.fr/23868599/)

914 74. Ranga A, Gobaa S, Okawa Y, Mosiewicz K, Negro A, Lutolf MP. 3D niche
915 microarrays for systems-level analyses of cell fate. *Nat Commun* [Internet]. 2014 Jul
916 14 [cited 2020 Jul 6];5. Available from: <https://pubmed.ncbi.nlm.nih.gov/25027775/>

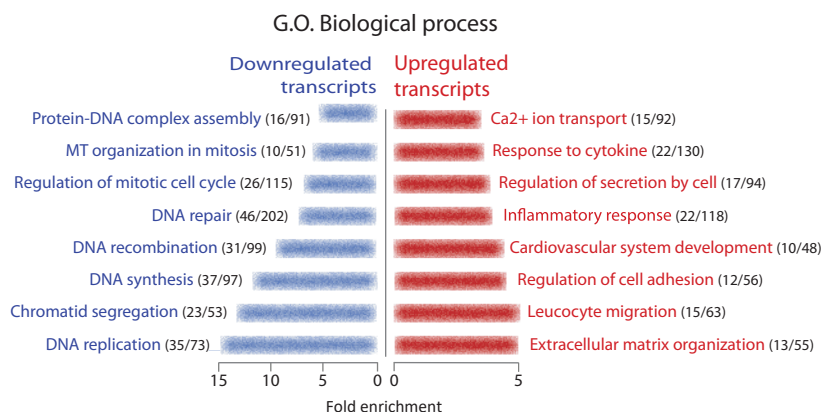
917 75. Lutolf MP, Lauer-Fields JL, Schmoekel HG, Metters AT, Weber FE, Fields GB, et al.
918 Synthetic matrix metalloproteinase-sensitive hydrogels for the conduction of tissue
919 regeneration: Engineering cell-invasion characteristics. *Proc Natl Acad Sci U S A*
920 [Internet]. 2003 Apr 29 [cited 2020 Jul 6];100(9):5413–8. Available from:
921 <https://pubmed.ncbi.nlm.nih.gov/12686696/>

922

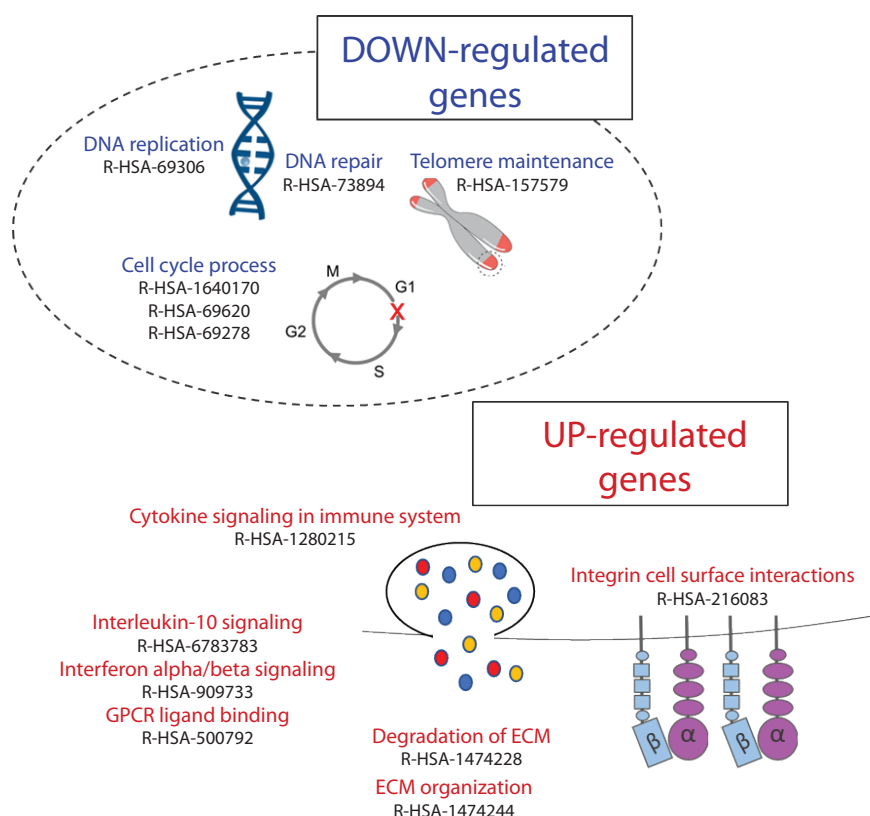
A



B



C



D

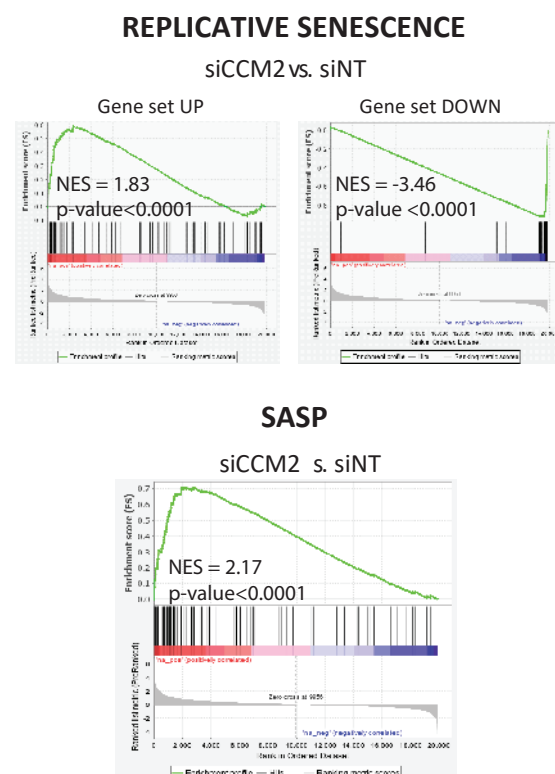


Figure 1: The loss of CCM2 turns on a SASP transcriptomic program.

(A) Gene Ontology enrichment analysis of cellular components in downregulated and upregulated genes in siCCM2 HUVEC compared to siNT HUVEC, bar graphs represent the fold enrichment. (B) Gene Ontology enrichment analysis of biological functions in downregulated and upregulated genes in siCCM2 HUVEC compared to siNT HUVEC, bar graphs represent the fold enrichment. (C) Schematic representation of the of enriched pathways in siCCM2 HUVEC with their reactome identification numbers. (D) GSEA profiles showing a significant normalized enrichment score (NES) of gene sets associated with replicative senescence (37) and SASP (39) in siCCM2 HUVEC transcriptome.

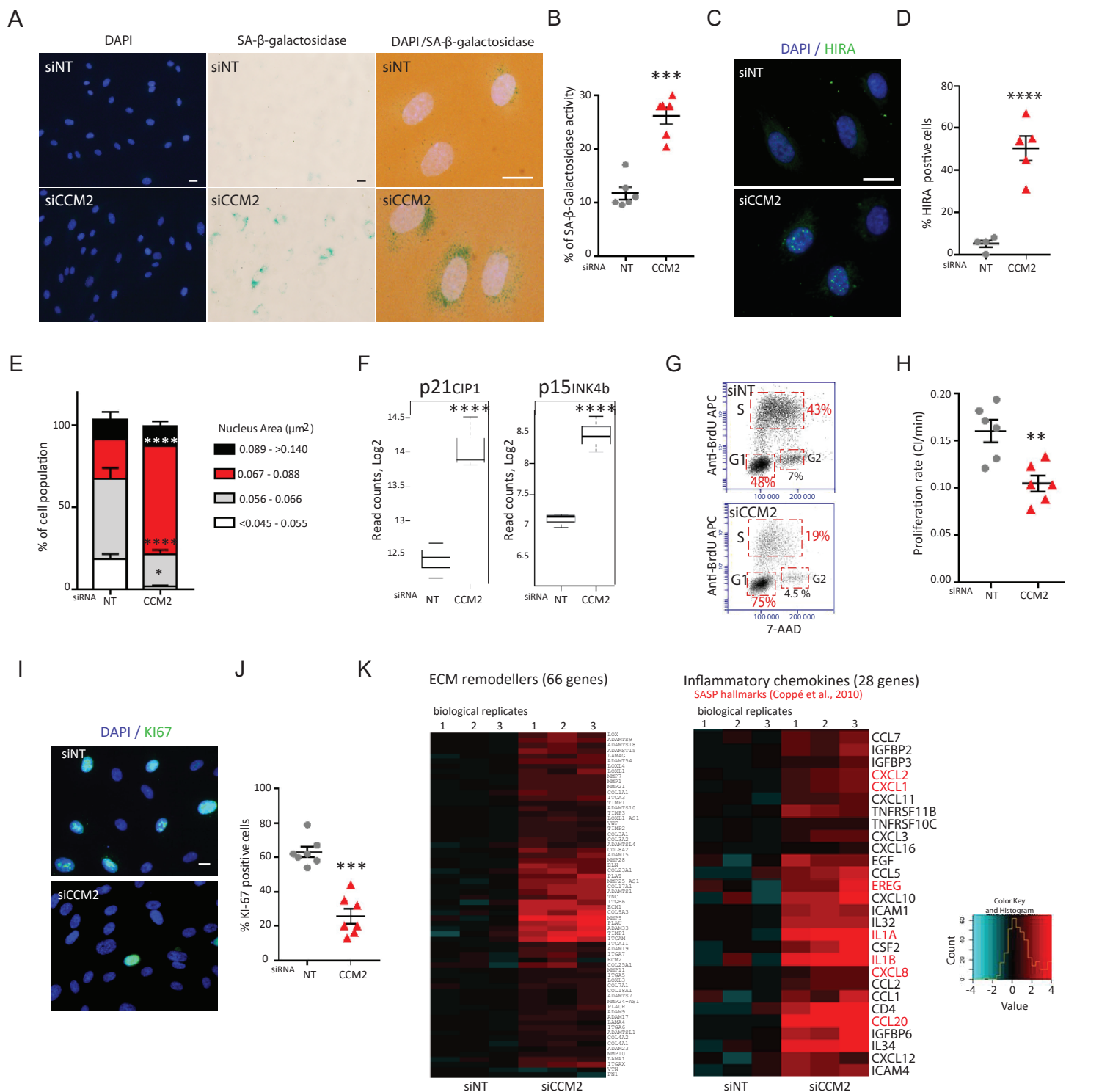


Figure 2: CCM2-depleted EC display hallmarks of SASP.

(A) Representative images of DAPI and SA-βgalactosidase staining of siNT and siCCM2 HUVEC. (Middle) Merge of DAPI and SA-β-galactosidase stainings at higher magnification. (B) Quantification of the % of positive cells for SA-β-galactosidase. Error bars are means ± SEM from 6 independent experiments. (C) Representative images of merged DAPI and HIRA stainings of siNT and siCCM2 HUVEC. (D) Quantification of the % of HIRA positive cells. Error bars are means ± SEM from 5 independent experiments. (E) Histogram of the cell population in function of their nucleus area. Error bars are means ± SEM from 4 independent experiments. (F) Boxplots of the read counts for p21/CIP1 and p15/INK4b mRNA. Error bars are means ± SEM from 3 independent experiments. (G) Representative plot showing BrdU incorporation as a function of total DNA content. The percentage of cells in each phase of the cell cycle is indicated. (H) Proliferation rate of siRNA transfected HUVEC measured by impedance using XCELLigence. Error bars are means ± SEM from 4 independent experiments. (I) Representative images of the proliferation marker Ki-67 staining (green) merged with DAPI staining. (J) Quantification of the percentage of cells positive for Ki-67 staining. Error bars are means ± SEM from 7 independent experiments. (K) Heatmap of expression of ECM remodelling proteins (left) (see Fig S4 for enlarged panel) and of SASP factors (right) over the 2 siRNA conditions, 3 biological replicates per condition. (*) P-value<0.05; (**) P-value<0.005; (***) P-value<0.0005; (****) P-value<0.00005. Scale bars are equal to 10 μm.

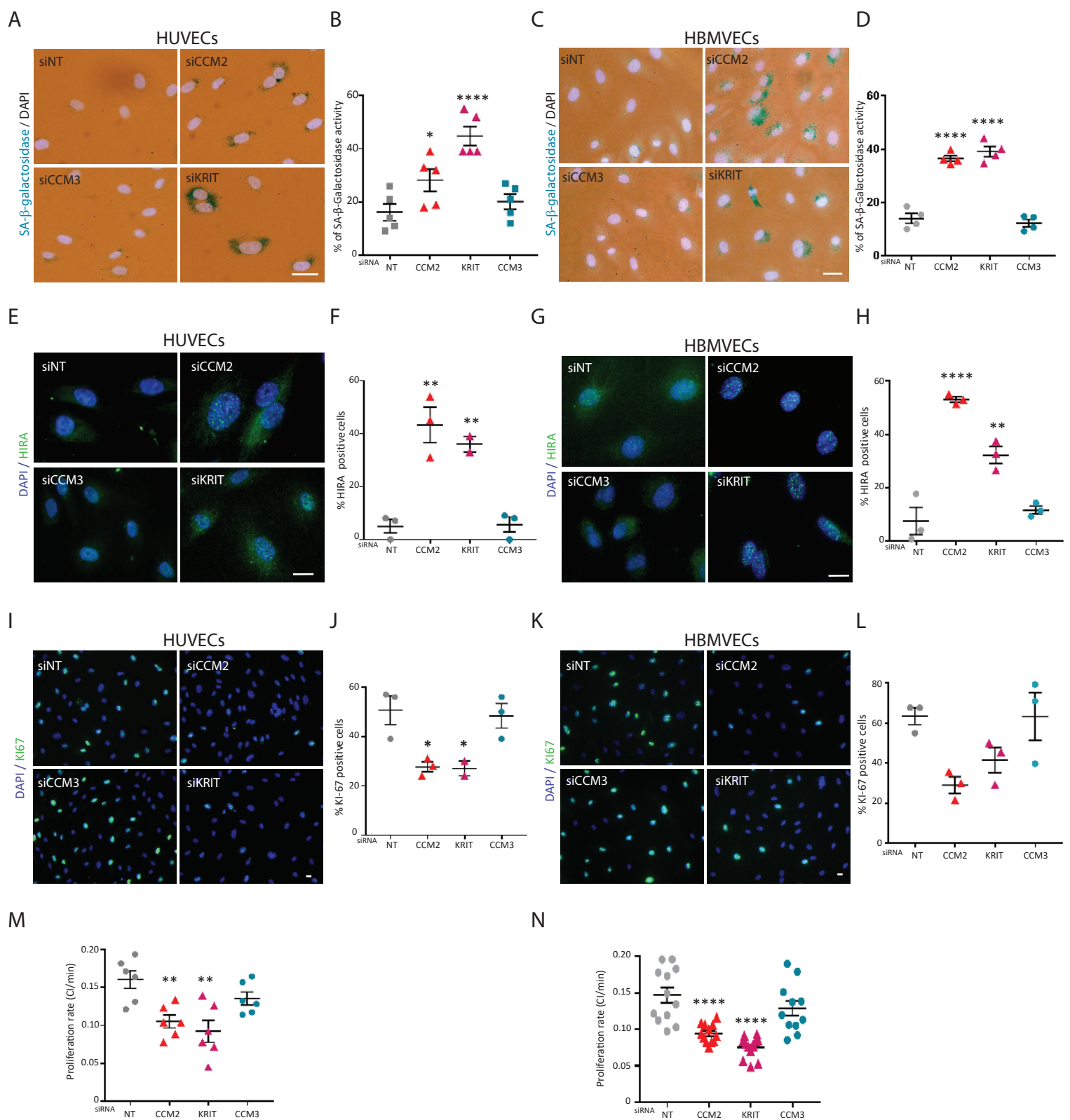


Figure 3: The loss of KRIT similarly to that of CCM2 leads to senescence in ECs whereas the loss of CCM3 does not.

Representative merged images of DAPI and SA-β-galactosidase stainings in HUVECs (A) and HBMVECs (C). Quantification of the % of positive cells for SA-β-galactosidase in HUVECs (B) and HBMVECs (D). Error bars are means \pm SEM from 5 (HUVECs) or 3 (HBMVECs) independent experiments. Representative images of merged DAPI and HIRA stainings for HUVECs (E) and HBMVECs (G). Quantification of the % of HIRA positive cells in HUVECs (F) and HBMVECs (H). Error bars are means \pm SEM from 3 (2 for KRIT) (HUVECs) and 3 (HBMVECs) independent experiments. Representative images of the proliferation marker Ki-67 staining (green) merged with DAPI staining in HUVECs (I) and HBMVECs (K). Quantification of the percentage of cells positive for Ki-67 staining for HUVECs (J) and HBMVECs (L). Error bars are means \pm SEM from 3 (2 for KRIT) (HUVECs) and 3 (HBMVECs) independent experiments. Proliferation rate of siRNA transfected HUVECs (M) and HBMVECs (N) measured by impedance using XCELLigence. Errors bars are means \pm SEM from 6 to 12 technical replicates over 3 independent experiments.

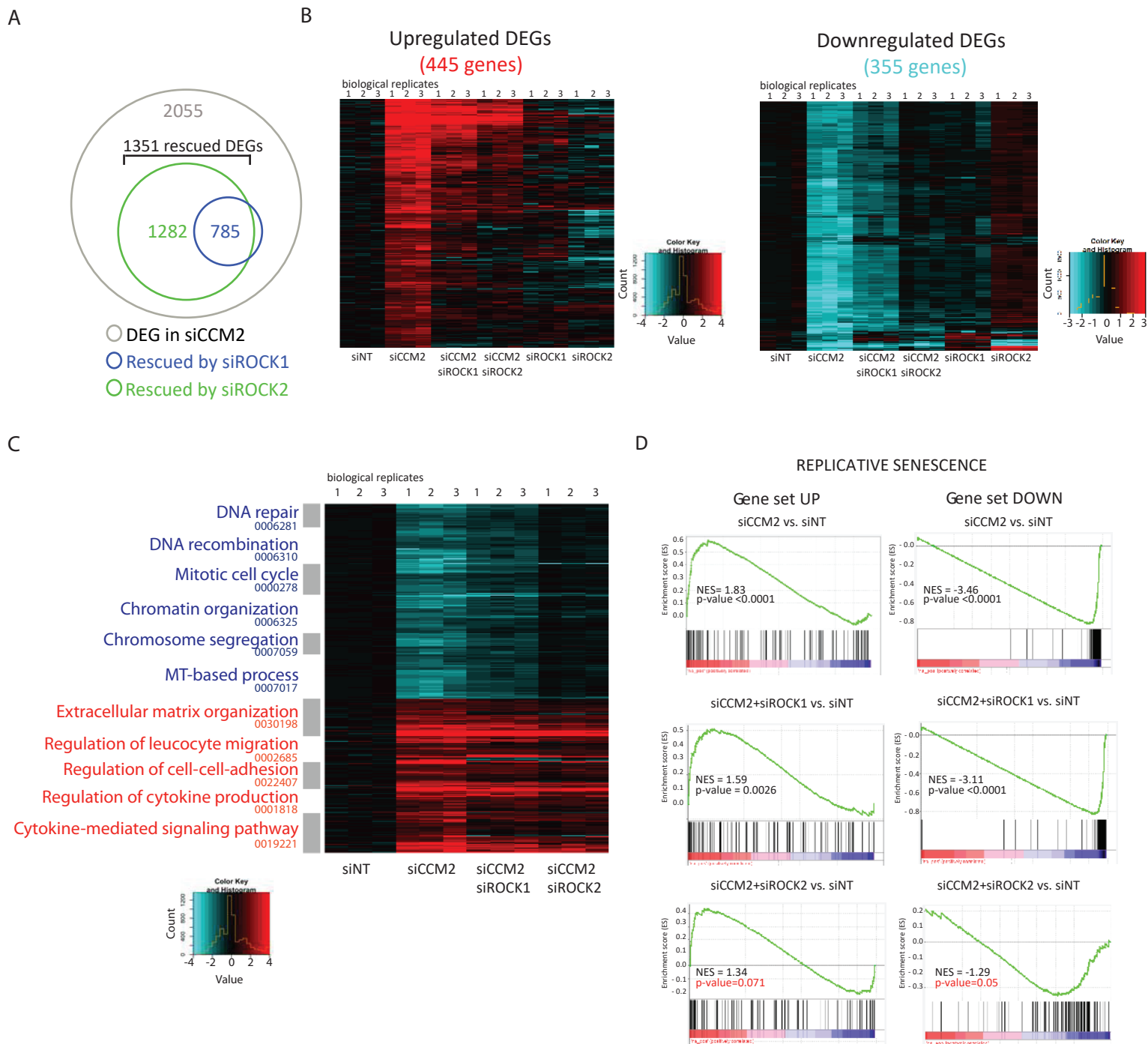


Figure 4: ROCK2 controls the SASP transcriptomic program of CCM2-depleted EC

(A) Venn diagrams showing overlap of DEGs with $FC \geq 2$; $P < 0.05$ in siCCM2 HUVEC (grey) with DEG rescued in siCCM2+siROCK1 (Blue) siCCM2+siROCK2 (Green). (B) Heatmap of the DEGs with $FC \geq 2$; $P < 0.05$ restored in common by ROCK1 and ROCK2. Upregulated (left) and downregulated (right) genes over the 6 siRNA conditions, 3 biological replicates per condition. (C) Clustered heatmap of GO enriched in up- and down-regulated genes in siCCM2 HUVEC. (D) GSEA enrichment plot showing the loss of significant enrichment in replicative senescence signature in siCCM2+ROCK2 but not in siCCM2+ROCK1 HUVEC transcriptome.

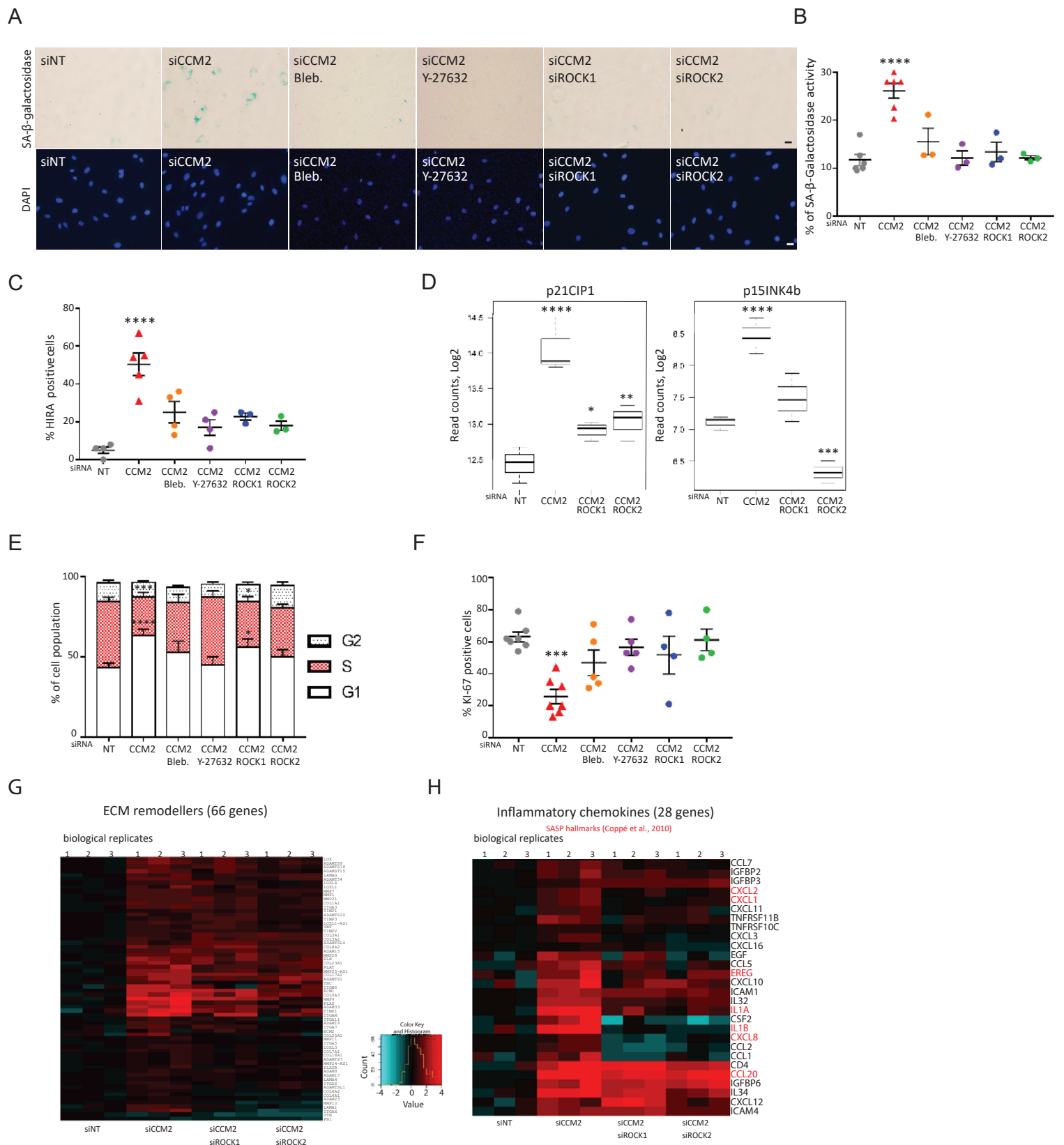
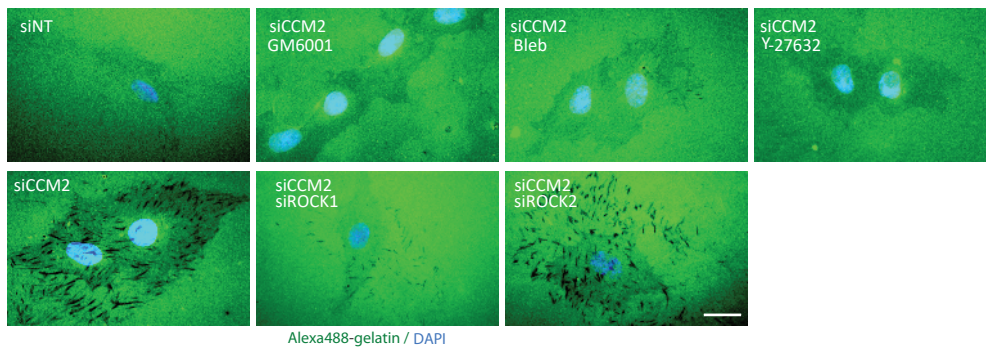


Figure 5: ROCKs dysfunctions induce premature senescence in CCM2-depleted ECs.

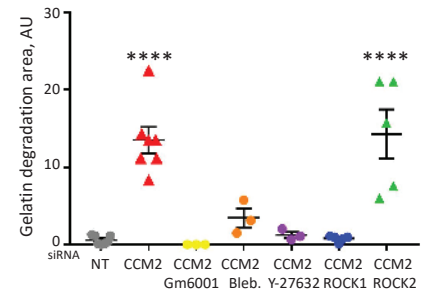
(A) Representative images of SA-β-galactosidase and DAPI stainings of siRNA-transfected HUVECs treated or not with blebbistatin or Y27632 at 10 μM. (B) Quantification of the % of positive cells for SA-β-galactosidase. Error bars are means ± SEM from 3 independent experiments. (C) Quantification of the % of HIRA positive cells in siRNA-transfected HUVECs treated or not with blebbistatin or Y27632. Error bars are means ± SEM from 4 (drug treatments) and 3 (ROCKs silencing) independent experiments. (D) Boxplots of the read counts for p21/CIP1 and p15/INK4b after depletion of ROCK1 or ROCK2. Error bars are means ± SEM from 3 independent experiments. (E) Quantification by BrdU assay of the percentage of cells in each phase of the cell cycle for siRNA-transfected HUVECs treated or not with blebbistatin or Y27632. Error bars are means ± SEM from 5 (drug treatments) and 8 (ROCKs silencing) independent experiments. (F) Quantification of the percentage of cells positive for Ki-67 staining. Error bars are means ± SEM from 5 (drug treatments) to 4 (ROCKs silencing) independent experiments. (G) Heatmap of expression of ECM remodelling proteins (left) and of SASP factors (right) over the 4 siRNA conditions, 3 biological replicates per condition. (*) P-value<0.05; (**) P-value<0.005; (***) P-value<0.0005; (****) P-value<0.00005. Scale bars are equal to 10 μm. Data for siNT and siCCM2 HUVECs are the same as in figure 2.

A

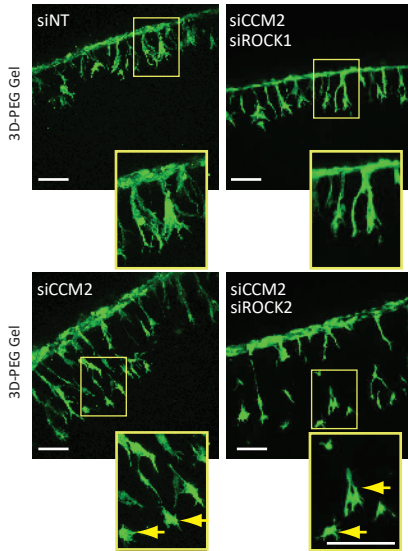


Alexa488-gelatin / DAPI

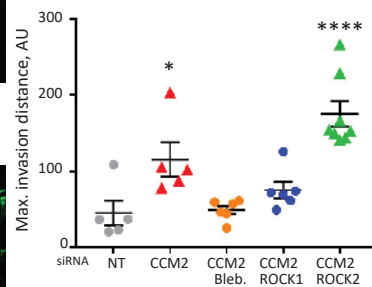
B



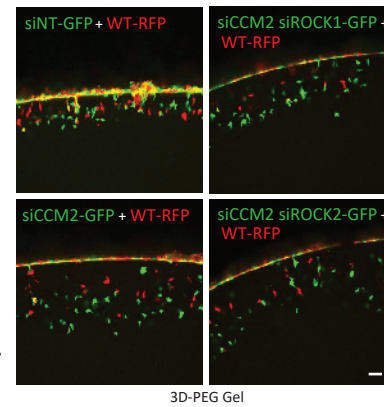
C



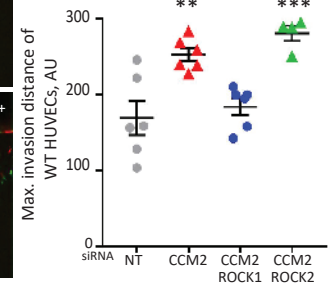
D



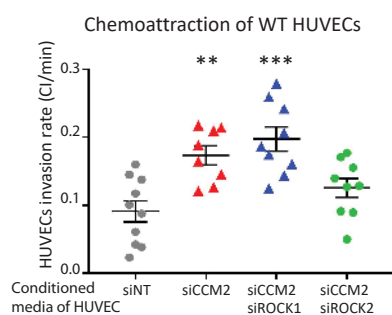
E



F



G



Chemoattraction of macrophages

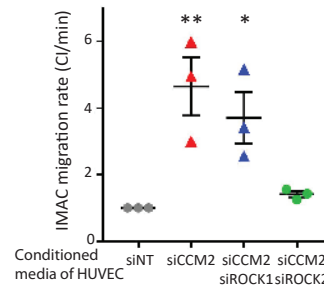
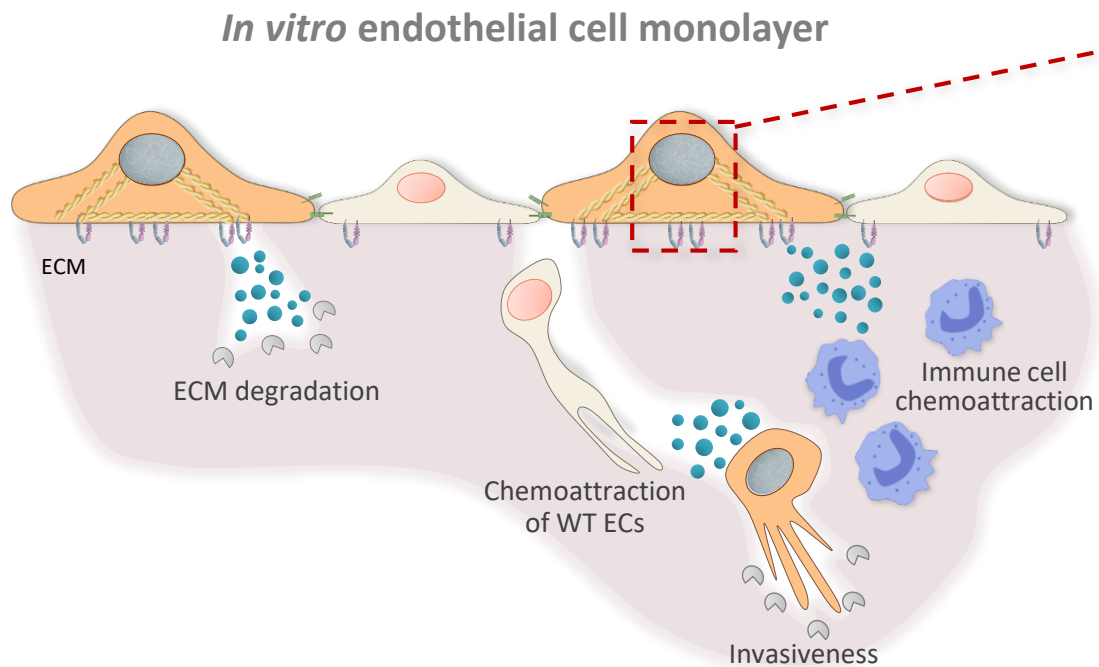
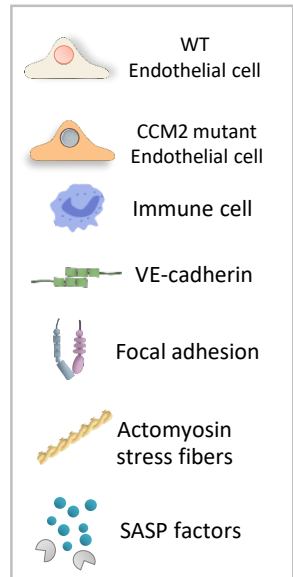


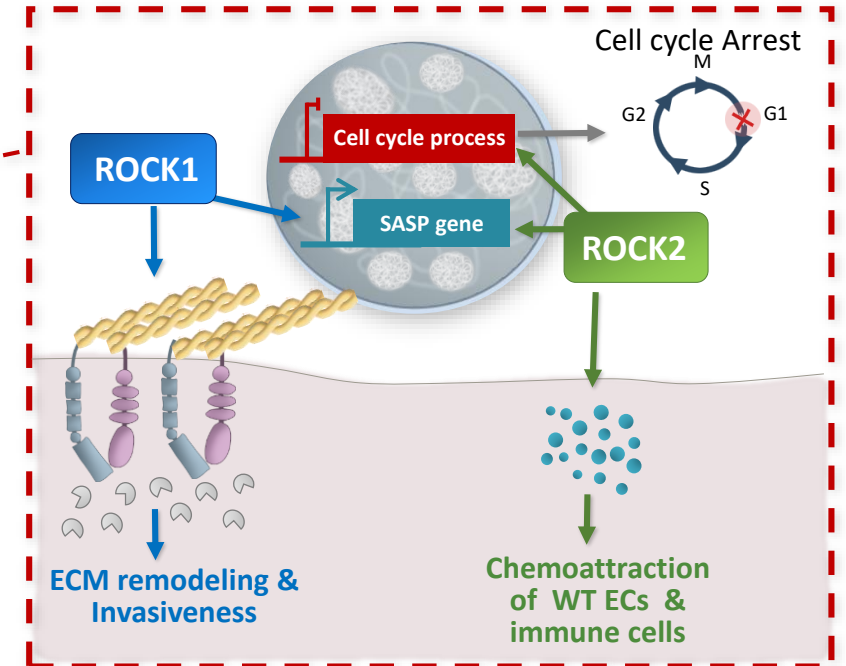
Figure 6: ROCK1 causes ECM degradation and invasion by CCM2-depleted HUVECs and neighbouring WT EC while ROCK2 causes chemo-attraction of WT ECs and macrophages.

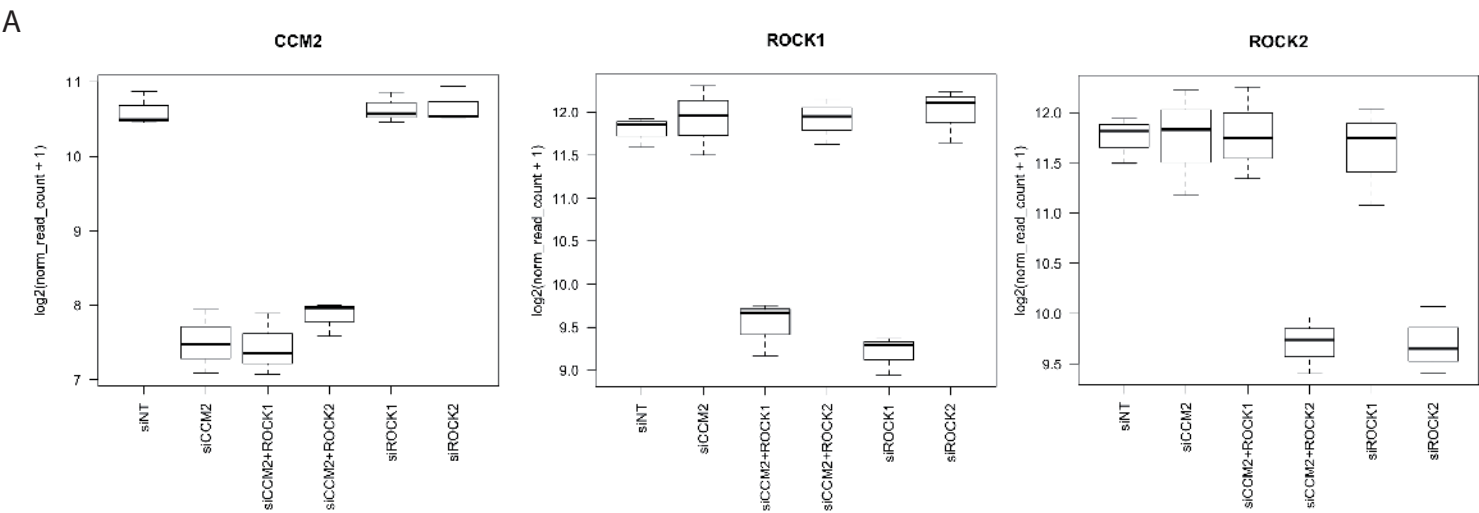
(A) Representative images of the degradation of fluorescent gelatin by siRNA transfected HUVECs treated or not with GM6001, blebbistatin or Y-27632. Scale bars, 10µm. (B) Quantification of the area of gelatin degradation. Error bars are means \pm SEM from 3 (drug treatments) or 5 (silencing of ROCKs) independent experiments. (C) Representative images of siRNA transfected GFP-HUVECs after invasion of 3D-PEG gels. Yellow squares are magnified zones of the images. Yellow arrows point at isolated invading cells. Scale bars, 50µm. (D) Quantification of the maximum invasion distance of siRNA transfected HUVECs treated or not with blebbistatin. Error bars are means \pm SEM from 3 independent experiments (2 to 3 technical replicates per condition) for siRNA transfected HUVECs and 2 for blebbistatin treated HUVECs. (E) Representative images of siRNA transfected GFP-HUVECs and RFP WT-HUVECs after invasion of 3D-PEG gels. Scale bar, 50µm. (F) Quantification of the maximum invasion distance of RFP WT-HUVECs. Error bars are means \pm SEM from 3 independent experiments (2 to 3 technical replicates per condition). (G) Quantification of the rate of invasion of WT HUVECs upon chemo-attraction by conditioned media of siRNA-transfected cells measured in a modified Boyden chamber in real time using xCELLigence. Error bars are means \pm SEM from 3 independent experiments (2-4 technical replicates per condition). (H) Quantification of the rate of transmigration of IMAC macrophages upon chemo-attraction by conditioned media of siRNA-transfected cells measured in a modified Boyden chamber in real time using xCELLigence. Error bars are means \pm SEM from 3 independent experiments.

(*) P-value<0.05; (**) P-value<0.005; (***) P-value<0.0005; (****) P-value<0.00005.



ROCKs-dependent Senescence-Associated with Secretory Phenotype





B

C

FigS1: Validation of the silencing of the target genes by siRNA in HUVECs and HBMVECs

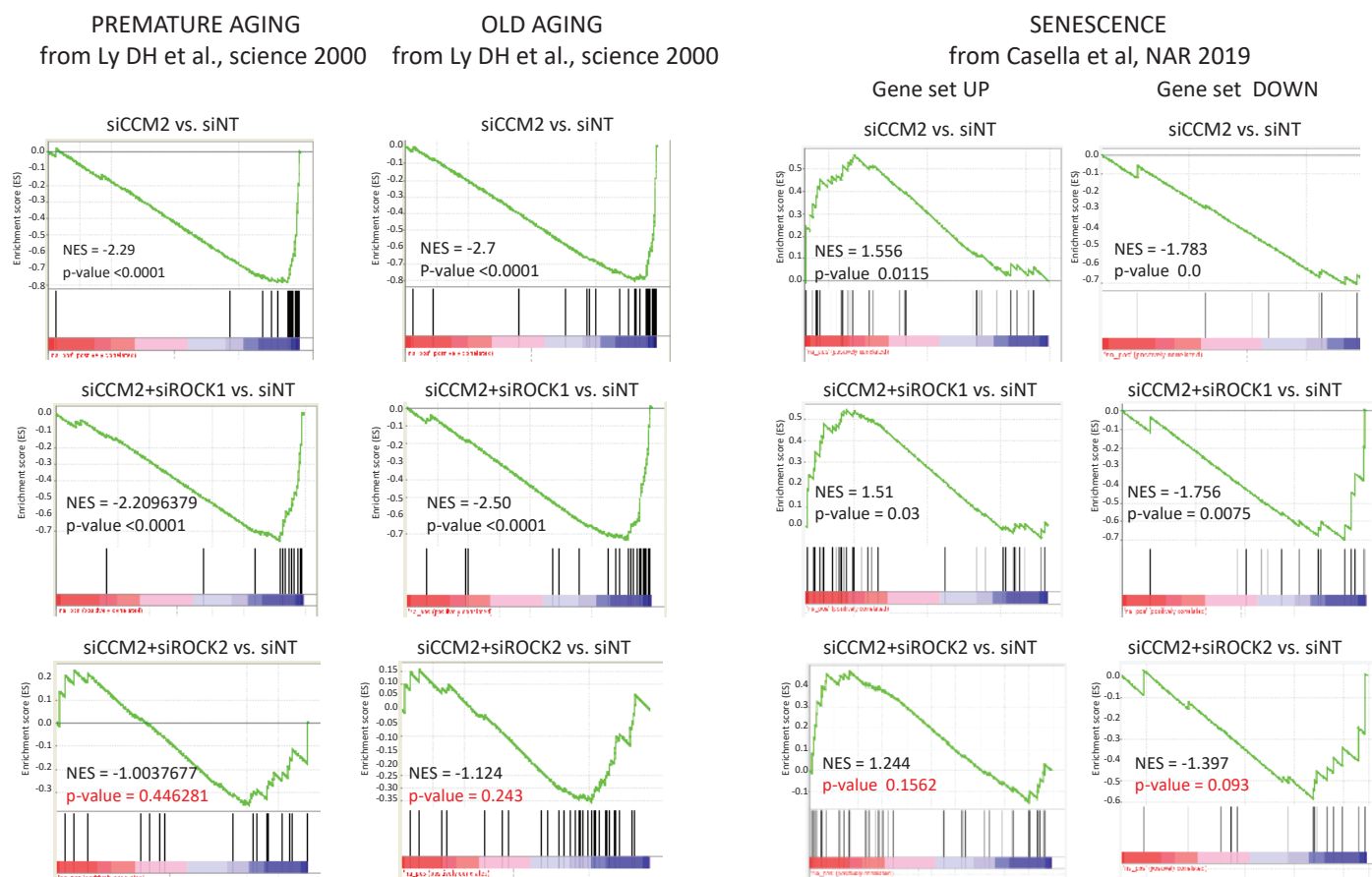
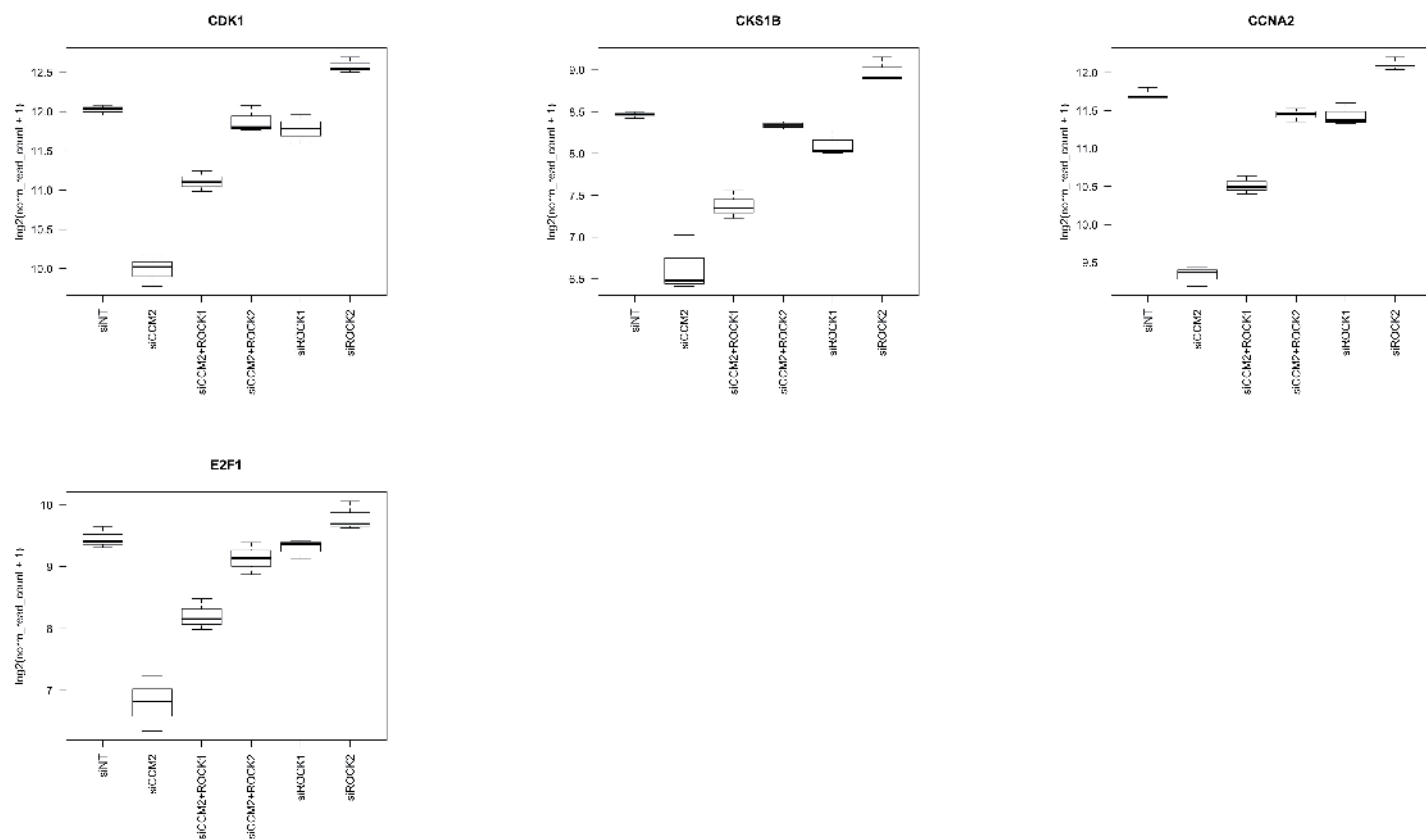


Fig S2: GSEA analyses using different gene sets of senescence.

Comparison of the enrichment in different senescence and SASP signatures(38,40) in siCCM2, siCCM2+ROCK1 and siCCM2+ROCK2.

Figure S2



FigS3: Boxplots of the expression level of cell cycle regulators
in the 6 siRNA conditions, 3 biological replicates per condition, as measured by RNA seq.

ECM remodellers (66 genes)

biological replicates

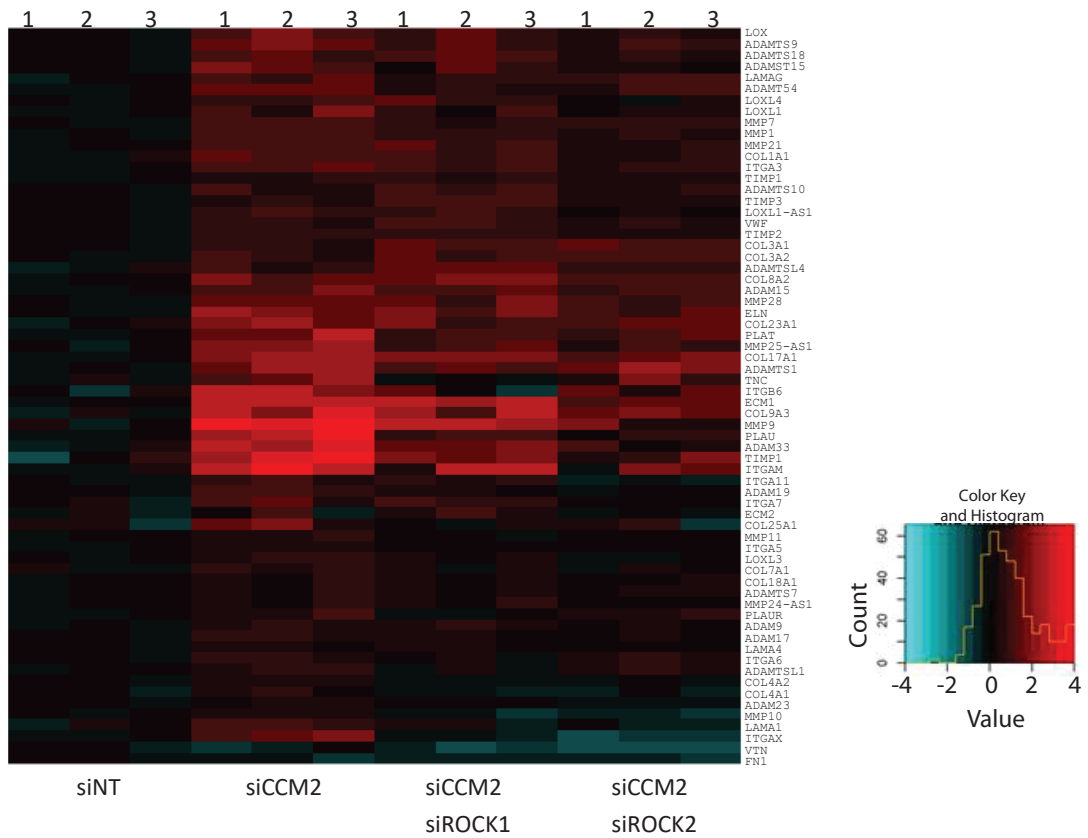
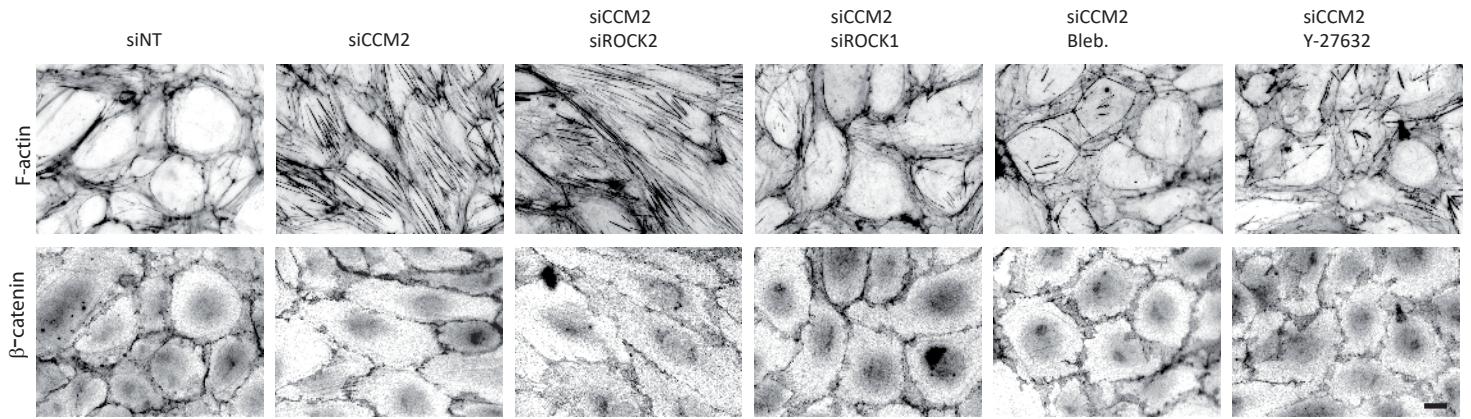


Fig S4 : Heatmap of expression of ECM remodelling proteins over the 4 siRNA conditions, 3 biological replicates per condition.

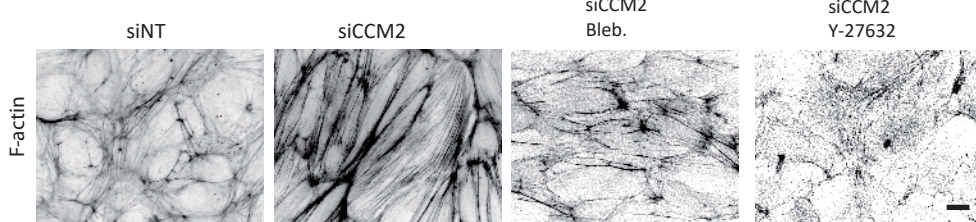
A

HBMVECs

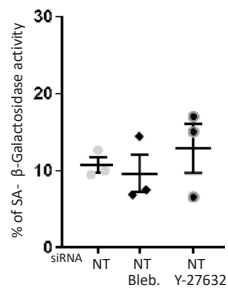


B

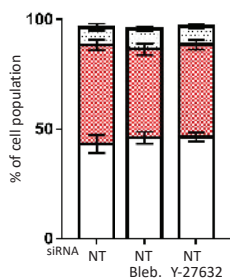
HUVECs



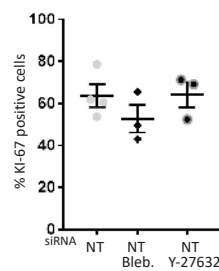
C



D



E



F

β1 integrin

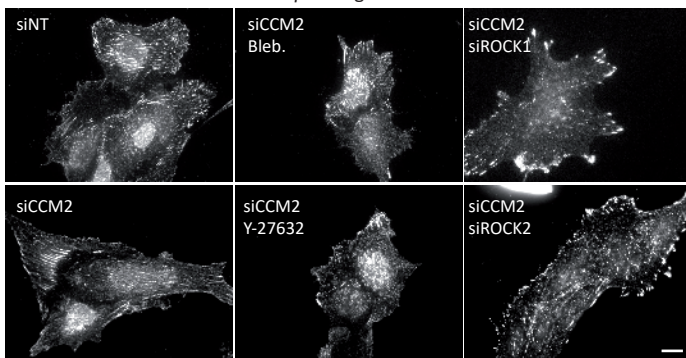


Fig S5: Effects of ROCKs silencing or drug treatments on the acto-adhesive phenotype of siCCM2 HBMVECs and HUVECs and on senescence marks in siNT HUVECs

(A) Representative immunofluorescence images of F-actin and β-catenin stainings in siRNA transfected HBMVECs. Scale bar 10 μm.

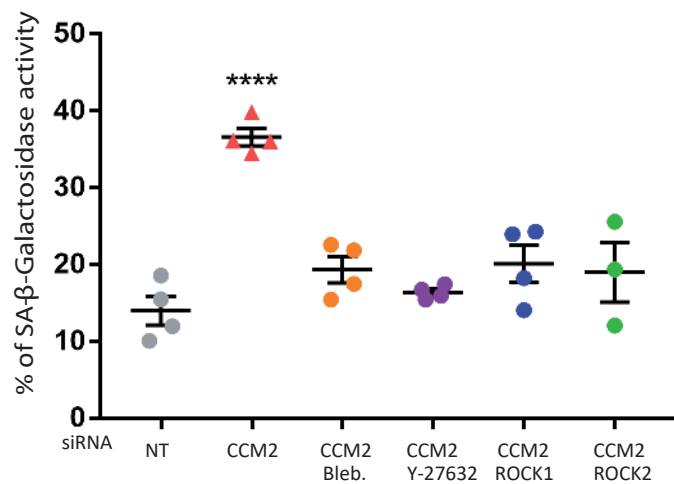
(B) Representative immunofluorescence images of the actin cytoskeleton of CCM2 transfected HUVECs treated or not with Blebbistatin or Y-27632, scale bar 10 μm. Effects these drugs on SA-β-galactosidase activity

(C) cell cycle progression (D) and Ki67 staining (E) of siNT HUVECs.

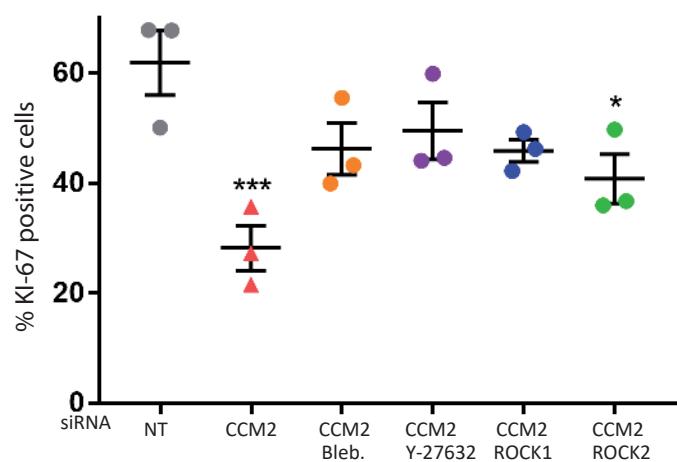
(F) Representative immunofluorescence images of β1 integrin staining in siRNA transfected HUVECs treated or not with Blebbistatin or Y-27632. Scale bar 10 μm

A

HBMVECs



B



C

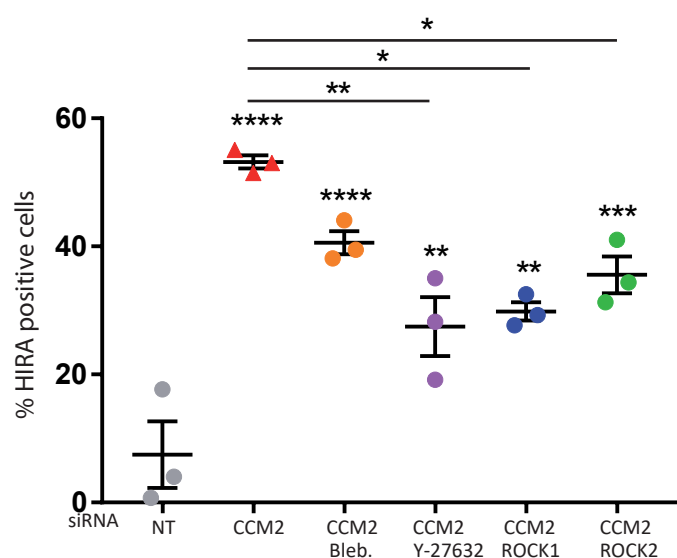


Figure S6: ROCKs dysfunctions induce senescence marks in CCM2-depleted HBMVECs.

(A) Quantification of the % of cells positive for SA-β-galactosidase in siRNA-transfected HBMVECs treated or not with blebbistatin or Y-27632. Error bars are means ± SEM from 3 independent experiments. (B) Quantification of the % of cells positive for Ki-67 staining in siRNA-transfected HBMVECs treated or not with blebbistatin or Y-27632. Error bars are means ± SEM from 3 independent experiments. (C) Quantification of the % of HIRA positive cells in siRNA-transfected HBMVECs treated or not with blebbistatin or Y-27632. Error bars are means ± SEM from 3 independent experiments. (*) P-value<0.05; (**) P-value<0.005; (***) P-value<0.0005; (****) P-value<0.00005. Data for siNT and siCCM2 HBMVECs are the same as in figure 3.

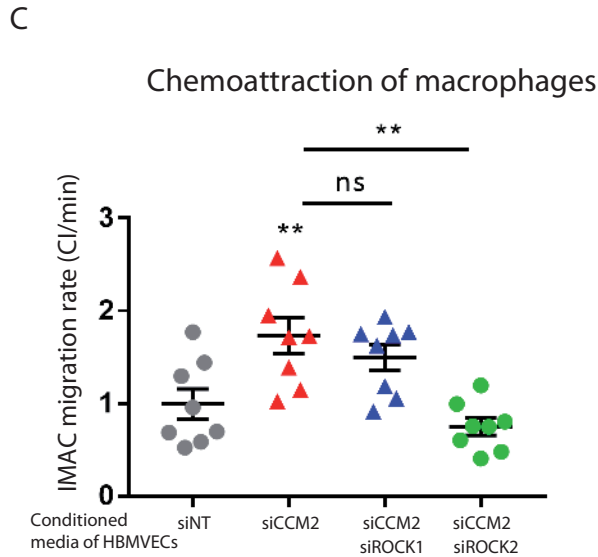
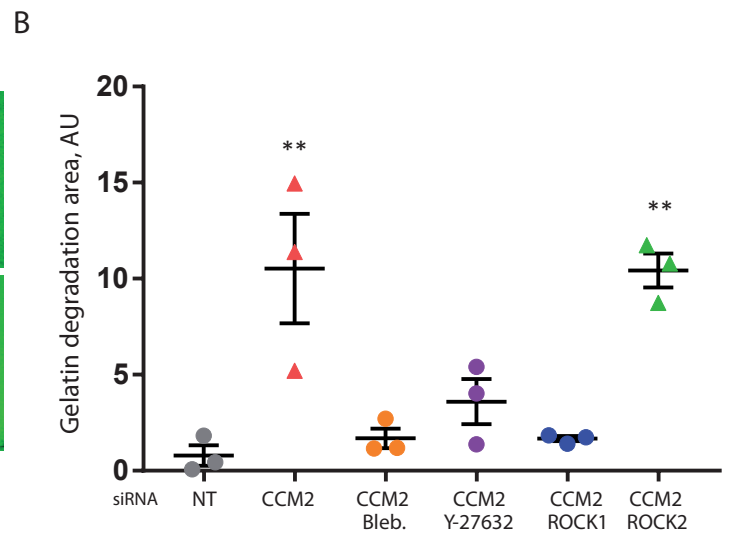
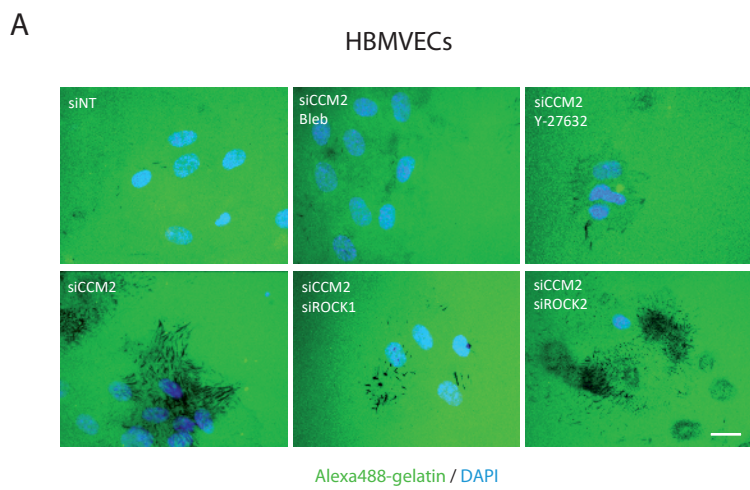
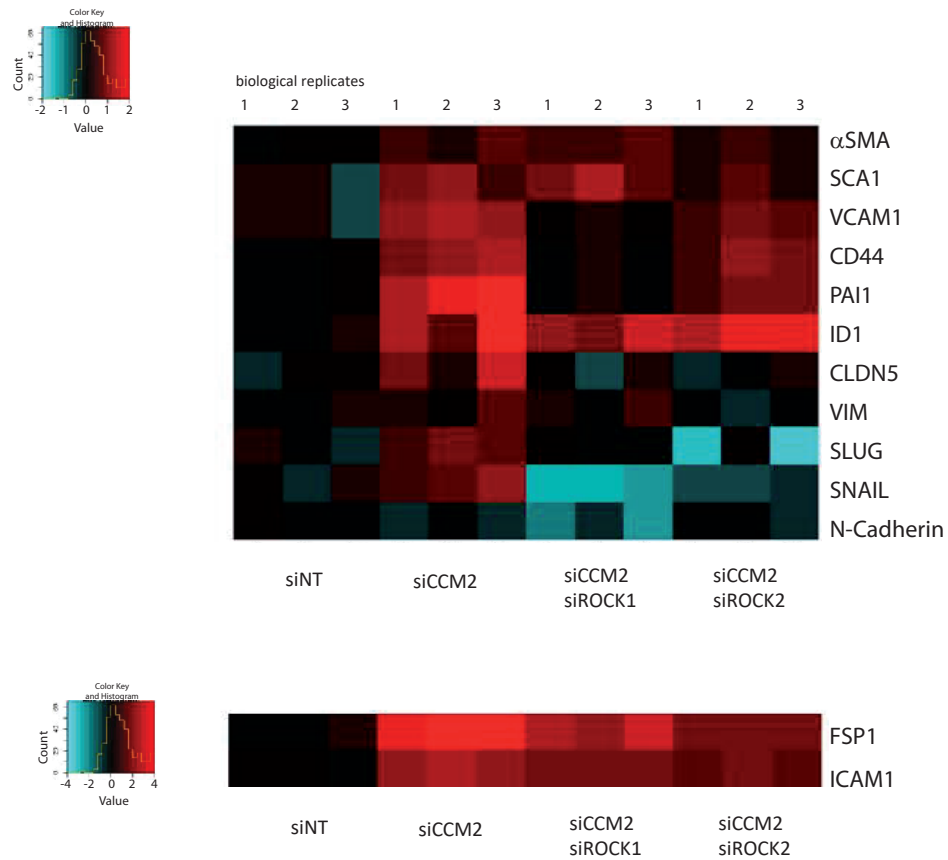


Figure S7 : As in HUVECs, ROCK1 causes ECM degradation by CCM2-depleted HBMVECs and ROCK2 causes chemo-attraction of macrophages.

(A) Representative images of the degradation of fluorescent gelatin by siRNA transfected HBMVECs treated or not with blebbistatin or Y-27632. Scale bars, 10 μ m. (B) Quantification of the area of gelatin degradation. Error bars are means \pm SEM from 3 drug treatments independent experiments. (C) Quantification of the rate of transmigration of IMAC macrophages measured in a modified Boyden chamber in real time using xCELLigence upon chemo-attraction by conditioned media of siRNA-transfected HBMVECs. Error bars are means \pm SEM from 3 independent experiments.

(*) P-value<0.05; (**) P-value<0.005.



FigS8: Heatmap of EndMT markers over the 4 biological conditions